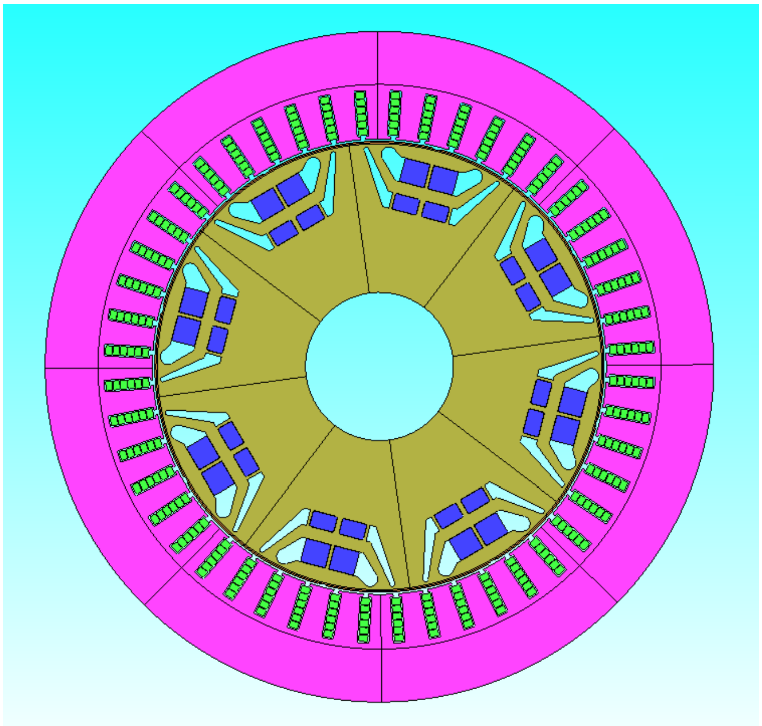

Performance Improvement of IPMSM with Sustainable Materials

Master's thesis in Master Programmes:
Sustainable Electric Power Engineering and Electromobility

Mahboubeh Ameri, Soroush Rezapour

Department of Electrical Engineering
Division of Electric Power Engineering

CHALMERS UNIVERSITY OF TECHNOLOGY
Gothenburg, Sweden 2026

www.chalmers.se

Performance Improvement of IPMSM with Sustainable Materials

Master of Science Thesis

Mahboubeh Ameri
Soroush Rezapour

Department of Electrical Engineering
Division of Electric Power Engineering
CHALMERS UNIVERSITY OF TECHNOLOGY
Göteborg, Sweden 2026

Performance Improvement of IPMSM with Sustainable Materials

Mahboubeh Ameri
Soroush Rezapour

CHALMERS
UNIVERSITY OF TECHNOLOGY

Department of Electrical Engineering
Division of Electric Power Engineering
CHALMERS UNIVERSITY OF TECHNOLOGY
Göteborg, Sweden 2026

Performance Improvement of IPMSM with Sustainable Materials
Mahboubeh Ameri
Soroush Rezapour

Supervisor: Siavash Sadeghpour, Rishabh Raj Volvo Car Corporation
Examiner: Torbjörn Thiringer, Department of Electrical Engineering

Department of Electrical Engineering
Division of Electric Power Engineering
Chalmers University of Technology
SE–412 96 Göteborg
Sweden
Telephone +46 (0)31–772 1000

Cover:
Illustration of an Interior Permanent Magnet Synchronous Motor (IPMSM)

Göteborg, Sweden 2026

Performance Improvement of IPMSM with Sustainable Materials
Mahboubeh Ameri
Soroush Rezapour

Department of Electrical Engineering
Division of Electric Power Engineering
Chalmers University of Technology

Abstract

This thesis investigates the redesign and optimization of an Interior Permanent Magnet Synchronous Motor (IPMSM) for electric vehicle traction applications using heavy rare-earth-free permanent magnet materials. The main objective is to improve demagnetization robustness under Active Short-Circuit (ASC) conditions while maintaining the required torque capability, efficiency, and cost performance.

Different magnet materials, rotor topologies, and machine configurations were evaluated using finite element simulations in JMAG. The study includes topology screening, ASC analysis, preliminary parametric optimization, and full-scale optimization using a genetic algorithm approach.

Based on the obtained simulation results, two candidate machine configurations were selected for further optimization and compared with the benchmark motor in terms of torque capability, efficiency, losses, material usage, and irreversible demagnetization behavior. In addition, sensitivity analysis and correlation studies were used to identify the most influential design parameters during the optimization process.

The results demonstrate that suitable rotor topology selection and electromagnetic optimization can significantly improve ASC robustness and reduce demagnetization sensitivity while maintaining the required traction motor performance using heavy rare-earth-free magnet materials.

Index Terms: IPMSM, rotor topology optimization, active short circuit, demagnetization robustness, electric vehicle traction, heavy rare-earth–free magnets, finite element analysis, flux weakening, torque density

Acknowledgements

We would like to thank Volvo Car Corporation and the whole of the Electric Driveline team for giving us the opportunity to do our Master's thesis with them. We are especially grateful for all the support and feedback during the whole project from our supervisors Siavash Sadeghpour, Rishabh Raj and examiner Torbjörn Thiringer.

Mahboubeh Ameri & Soroush Rezapour
Göteborg, Sweden, 2026

Contents

tikz float

Chapter 1

Introduction

1.1 Problem background

Interior Permanent Magnet Synchronous Motors (IPMSMs) are widely used in electric vehicle traction systems because they can provide high torque density, high efficiency, and good performance over a wide speed range [1]. These features are important for electric vehicles, where the motor must provide high torque at low speed for vehicle launch and acceleration, while also operating efficiently at higher speeds.

In an IPMSM, the magnets are placed inside the rotor. This structure makes it possible to use both magnet torque and reluctance torque. As a result, IPMSMs can achieve high efficiency and good flux-weakening capability, which is necessary for traction motors operating over a wide speed range.

However, the use of permanent magnets also creates several challenges. Many high-performance traction motors use rare-earth magnets because of their strong magnetic properties. These materials can provide high torque and compact motor design, but they are also linked to high material cost, supply chain uncertainty, and environmental concerns [2]. For this reason, there is a strong interest in reducing the dependency on rare-earth materials and developing more sustainable motor designs.

One possible solution is to use heavy rare-earth-free permanent magnets. These magnets can reduce material dependency and cost, but they may have weaker magnetic properties or lower demagnetization resistance compared with stronger magnet grade. This means that the motor geometry must be carefully redesigned to maintain the required torque and efficiency while avoiding irreversible demagnetization.

Demagnetization is a critical issue in IPMSMs. During normal operation, high current and high temperature can reduce the magnetic strength and demagnetization resistance of the magnets. Under fault conditions, the risk becomes even higher. One important fault case in electric vehicle traction systems is Active Short-Circuit (ASC). During ASC, large demagnetizing fields can appear inside the rotor and may cause permanent magnet damage [3]. If irreversible demagnetization occurs, the motor can lose torque capability, and thus its performance degrades.

Therefore, a motor design that works well only under normal operating conditions is not sufficient. The design must also be robust under fault conditions. In this thesis, the focus is on improving the performance and demagnetization robustness of the studied benchmark IPMSM by investigating alternative heavy rare-earth-free magnet materials, rotor topologies, and machine configurations. The goal is to find a design that can maintain the required performance while reducing cost and improving robustness against demagnetization.

1.2 Previous work

Previous studies have investigated different approaches to reduce the dependency on rare-earth materials in IPMSMs. One approach is to combine weaker magnetic materials with stronger permanent magnets in order to reduce the amount of critical magnetic material while still maintaining acceptable motor performance. For example, some studies have investigated low-coercivity materials such as iron nitride magnets together with standard permanent magnets. In these designs, the stronger magnets can support the weaker magnets and help reduce the risk of demagnetization [4].

Other studies have focused on rotor topology optimization. Different rotor structures, such as V-shaped, VV-shaped, and U-shaped topologies, have been studied to improve torque density, air-gap flux distribution, torque ripple, and flux-weakening capability. Multi-layer rotor structures can increase the reluctance torque contribution and improve the use of the magnetic flux inside the rotor. These improvements can help the motor reach higher torque or better efficiency [5].

However, many previous studies mainly focus on normal operating conditions. In many cases, fault conditions such as Active Short-Circuit are not fully considered. This is an important limitation because ASC can create strong demagnetizing fields and may lead to irreversible magnet damage. Therefore, a rotor design that performs well during normal operation may still be weak under fault conditions.

Another limitation is that many studies focus mainly on electromagnetic performance, such as torque and efficiency, while cost, magnet material selection, and demagnetization robustness are not always considered together. For electric vehicle traction motors, these aspects should be evaluated at the same time because the final design must be practical, robust, and cost-efficient.

This thesis builds on previous work by considering rotor topology, magnet material, and machine configuration together. The study focuses on the studied benchmark IPMSM and investigates whether weaker and more cost-efficient heavy rare-earth-free magnets can be used while maintaining the required torque performance and improving demagnetization robustness under ASC conditions.

1.3 Purpose

The purpose of this thesis is to investigate whether the performance of the studied benchmark IPMSM can be maintained, or further improved, by replacing the existing heavy rare-earth-free magnet with a weaker and more cost-efficient heavy rare-earth-free magnet. Although the benchmark motor already uses a heavy rare-earth-free magnet, the replacement magnet has weaker magnetic characteristics and different demagnetization behavior. Therefore, the machine design must be improved to compensate for the weaker magnet properties.

The work focuses on redesigning both rotor-related and selected stator-related parameters. Different rotor topologies are investigated together with different machine configurations in order to understand how magnet arrangement, rotor geometry, stator parameters, slot number, hairpin numbers, and parallel paths affect torque capability, efficiency, and demagnetization behavior.

The analysis is carried out using Finite Element Method (FEM) simulations in JMAG. This simulation-based approach makes it possible to evaluate the electromagnetic performance of the benchmark and redesigned models under normal operating conditions and Active Short-Circuit (ASC) fault conditions.

The final goal is to identify motor designs that can maintain the required torque and efficiency while reducing cost and improving robustness against irreversible demagnetization. In this way, the thesis contributes to the development of practical and cost-efficient IPMSM solutions for electric vehicle traction applications.

Chapter 2

Fundamental Theory and Analytical Background

2.1 Permanent Magnet Materials and Sustainability Background

Permanent magnet materials have an important effect on the performance, cost, and sustainability of IPMSMs. Many high-performance traction motors use rare-earth permanent magnets because they provide high magnetic strength and good torque capability. However, some rare-earth materials, especially heavy rare-earth elements, are associated with high cost, supply chain uncertainty, and environmental concerns.

Heavy rare-earth-free magnets can be a more attractive option from a sustainability and cost point of view. By reducing the dependency on heavy rare-earth elements, the motor design can become less sensitive to material availability and price variation. This is especially important for electric vehicle traction motors, where large-scale production requires stable and cost-effective material solutions.

In this thesis, heavy rare-earth-free magnet materials are investigated as alternatives for the studied IPMSM. These magnets may have lower coercivity or different demagnetization behavior compared with stronger magnet grades. Therefore, the rotor topology, magnet arrangement, and machine configuration must be improved to maintain the required torque and efficiency while also achieving the benefits of lower cost, improved sustainability, and reduced supply chain dependency [18].

2.2 Fundamental Electromagnetic Equations

The operation of an electrical machine is based on fundamental electromagnetic principles. In the stator windings, current produces a magnetic field, which creates magnetic flux in the magnetic circuit. According to Ampere's law, the relationship between the enclosed current and the magnetic field intensity can be expressed as

$$I_{\text{encl}} = \oint \frac{B}{\mu}\, dl = \int J_s \, dS \tag{1}$$

where B is the magnetic flux density, μ is the magnetic permeability, and J_s is the current density. The magnetic flux Φ through a surface S is defined as the integral of the magnetic flux density over that surface

$$\Phi = \int_S B \cdot dS \tag{2}$$

For a simplified uniform magnetic field, the flux can be written as

$$\Phi = BA \tag{3}$$

where A is the effective cross-sectional area. The flux linkage Ψ is an important parameter in electrical machines and is related to the current and inductance by

$$L = \frac{\Psi}{I} \tag{4}$$

where L is the inductance and I is the current.

The induced electromotive force is described by Faraday's law of induction. It states that the induced voltage is proportional to the rate of change of flux linkage

$$e_m = -\frac{d\Psi}{dt} \tag{5}$$

Considering the resistive and inductive effects of the stator winding, the terminal voltage can be written in a simplified form as

$$v = Ri + L\frac{di}{dt} \tag{6}$$

where R is the winding resistance, i is the current, and L is the inductance.

In an IPMSM, the permanent magnets inside the rotor provide the main magnetic flux. Since the magnets are buried inside the rotor, the magnetic reluctance is different along the direct and quadrature axes. This leads to different inductances, L_d and L_q, which is one of the key characteristics of the IPMSM structure [1]. This concept is further explained using the d-q reference frame in the following sections.

2.3 Mathematical Modeling of the IPMSM

The Interior Permanent Magnet Synchronous Motor (IPMSM) is a type of synchronous motor in which the permanent magnets are placed inside the rotor. The stator windings produce a rotating magnetic field, while the rotor magnets provide the main excitation flux. The interaction between the stator current and the rotor magnetic field produces electromagnetic torque.

The mathematical model of an IPMSM is usually developed in the rotating d-q reference frame. This is because the three-phase stator variables are time-varying in the abc frame, while they can be represented as almost constant quantities in the d-q frame under steady-state conditions. This makes the analysis of voltage, current, flux, and torque easier.

In an IPMSM, the rotor has magnetic saliency because the permanent magnets are embedded inside the rotor. As a result, the magnetic reluctance is different along the d-axis and q-axis. This causes the d-axis inductance L_d and q-axis inductance L_q to be different. This characteristic allows the IPMSM to produce both magnet torque and reluctance torque.

In this thesis, the mathematical model is used as a theoretical basis for understanding the FEM simulation results obtained in JMAG. It also helps to explain the effects of magnetic material selection, current angle, torque production, field weakening, and demagnetization behavior in the studied IPMSM [9, 10].

2.4 d–q Axis Theory

The d-q axis theory is used to simplify the analysis and control of synchronous machines. In this method, the three-phase stator variables are transformed into two rotating axes: the direct axis and the quadrature axis.

The direct axis, or d-axis, is aligned with the rotor magnetic flux. The quadrature axis, or q-axis, is perpendicular to the d-axis. Therefore, the stator current can be represented by two components: the d-axis current i_d and the q-axis current i_q.

The d-axis current mainly affects the magnetic flux of the machine. It is especially important for field weakening and reluctance torque production. The q-axis current mainly contributes to the magnet torque produced by the permanent magnets.

This representation provides a useful framework for studying torque production and motor control. It is also important for control methods such as Maximum Torque Per Ampere (MTPA), because the torque of an IPMSM depends on both i_d and i_q [1, 9]. Figure 2.1 illustrates the d-q reference frame, where the stator current vector is divided into the d-axis current component i_d and the q-axis current component i_q.

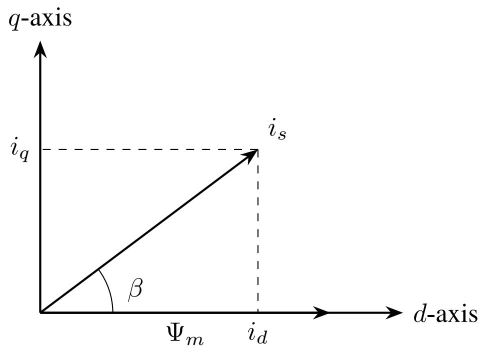

Figure 2.1: Stator current vector and its d-axis and q-axis components in the d-q reference frame.

2.5 Torque Production Analysis

The electromagnetic torque T_e in an IPMSM is produced by the interaction between the stator current vector and the rotor magnetic field. In the d-q reference frame, the torque can be expressed as

$$T_e = \frac{3}{2} p_p \left(\Psi_m i_q + (L_d - L_q) i_d i_q \right) \tag{7}$$

where p_p is the number of pole pairs, Ψ_m is the permanent magnet flux linkage, L_d and L_q are the d-axis and q-axis inductances, and i_d and i_q are the d-axis and q-axis current components.

The first term, $\Psi_m i_q$, represents the magnet torque. This torque is produced by the interaction between the permanent magnet flux and the q-axis current. The second term, $(L_d - L_q) i_d i_q$, represents the reluctance torque. This torque is produced because of the saliency of the rotor and the difference between L_d and L_q.

In most IPMSM structures, the q-axis inductance is higher than the d-axis inductance. Therefore, by applying a suitable negative d-axis current, the reluctance torque can support the magnet torque. This allows the motor to produce higher torque with better efficiency compared with a surface-mounted PMSM.

The combination of magnet torque and reluctance torque is one of the main advantages of IPMSMs. This dual-source torque production makes them suitable for high-performance electric drive applications, especially where high efficiency and wide speed range are required [1, 10].

2.6 Maximum Torque Per Ampere (MTPA)

The Maximum Torque Per Ampere (MTPA) method is an optimization control strategy used to produce the required torque with the minimum possible stator current. Since copper losses are proportional to the square of the current, reducing the current for a given torque can improve the efficiency of the motor.

In an IPMSM, the same torque can be achieved by different combinations of d-axis and q-axis currents. However, not all current combinations are efficient. The MTPA strategy finds the optimal current vector that gives the maximum torque for a fixed current magnitude.

The stator current magnitude can be written as

$$|i_s| = \sqrt{i_d^2 + i_q^2} \tag{8}$$

The d-axis and q-axis current components can also be expressed using the current angle β

$$i_d = |i_s| \cos \beta \tag{9}$$

$$i_q = |i_s| \sin \beta \tag{10}$$

where $|i_s|$ is the stator current magnitude and β is the current angle.

In the MTPA strategy, the current angle is selected so that the required torque is produced with the minimum possible stator current. The optimal current angle depends on the machine parameters, especially the permanent magnet flux linkage and the d-axis and q-axis inductances. In practical IPMSMs, these parameters may change because of magnetic saturation, temperature variation, and material properties. Therefore, the MTPA trajectory is often evaluated using FEM simulations or experimental results [1]. The MTPA strategy selects a suitable current vector in the d-q plane to produce the required torque with minimum current, as shown in Figure 2.2.

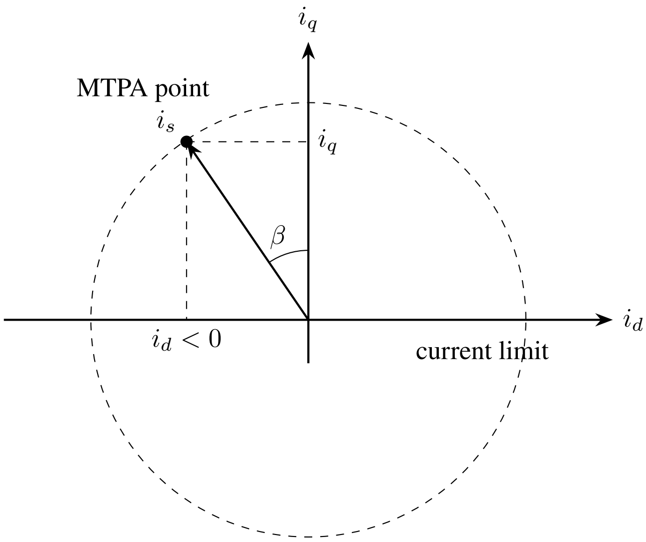

Figure 2.2: Current vector representation for MTPA operation in the d-q plane.

2.7 Field Weakening Operation

Field weakening is used to extend the speed range of an IPMSM beyond the base speed. At low and medium speeds, the motor can usually operate in the constant torque region, and the required stator voltage remains below the inverter voltage limit. In this region, the MTPA strategy can be used to produce the required torque with minimum current [11].

As the rotor speed increases, the back electromotive force, or back-EMF, also increases. This is because the induced voltage is related to the rate of change of flux linkage. When the motor reaches the base speed, the required voltage becomes close to the maximum voltage that the inverter can provide. Above this speed, the motor cannot continue to increase speed without reducing the effective air-gap flux [12].

To operate above the base speed, a negative d-axis current is applied. This current produces a magnetic field that partly opposes the permanent magnet flux. As a result, the effective flux linkage is reduced, which lowers the back-EMF and allows the motor to operate at higher speeds without exceeding the inverter voltage limit. However, this also reduces the available torque as the speed increases.

Therefore, field weakening is a trade-off between speed extension and torque capability. It is important in traction applications because electric vehicle motors must operate over a wide speed range. The general operating regions of a traction motor are shown in Figure 2.3.

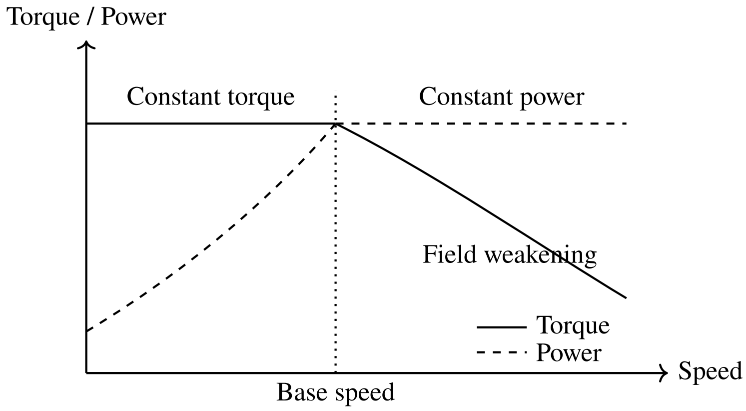

Figure 2.3: Typical torque and power regions during field weakening operation.

In this thesis, field weakening is relevant because the studied IPMSM must satisfy traction requirements over a wide speed range. The d-axis current, magnet flux linkage, and machine inductances influence the field weakening capability. Therefore, the rotor topology, magnet material, and machine configuration can affect not only the peak torque but also the high-speed performance of the motor.

2.8 Loss Mechanisms in High-Speed Electrical Machine

Losses in high-speed electrical machines are important because they affect efficiency, temperature rise, and the reliability of the machine. In traction motors, these losses must be considered carefully since the machine operates over a wide speed and torque range.

The main loss components considered in this study are copper loss, iron loss, and magnet eddy current loss. Copper loss occurs in the stator windings due to the winding resistance and current flow. At higher frequencies, additional effects such as skin effect and proximity effect can increase the effective resistance and lead to higher winding losses.

Iron loss occurs in the stator and rotor core due to the variation of magnetic flux. It mainly includes hysteresis loss and eddy current loss. These losses increase with frequency and flux density, so they become more important during high-speed operation.

Magnet eddy current loss occurs in the permanent magnets due to time-varying magnetic fields, which can be caused by stator slotting effects, current harmonics, and inverter-related harmonics. This loss can create local heating in the magnets and may affect the thermal behavior and demagnetization robustness of the machine.

In this thesis, understanding these loss mechanisms is useful for comparing the benchmark model and the redesigned candidates. The selected magnet material, rotor geometry, and machine configuration can influence the total losses and therefore affect the final efficiency of the studied IPMSM [13, 14].

2.9 Demagnetization Mechanisms

Demagnetization is an important limitation in permanent magnet machines, especially when the machine operates under high current or high temperature conditions. In an IPMSM, the permanent magnets are placed inside the rotor and are exposed to the magnetic field produced by the stator current. If this field acts against the magnetization direction of the magnets, it can reduce the magnet flux and weaken the motor performance.

In general, demagnetization can be reversible or irreversible. Reversible demagnetization means that the magnet can recover when the external condition is removed. Irreversible demagnetization means that part of the magnetization is permanently lost, which can reduce the torque capability of the machine [6].

Temperature also has an important influence on demagnetization. When the magnet temperature increases, the resistance of the magnet against demagnetizing fields decreases. Therefore, demagnetization analysis at elevated temperature is important for traction machines, especially when weaker heavy rare-earth-free magnets are used [8].

Figure 2.4 shows a simplified B-H demagnetization curve of a permanent magnet. The figure illustrates the safe operating region, the knee point, and the irreversible demagnetization region.

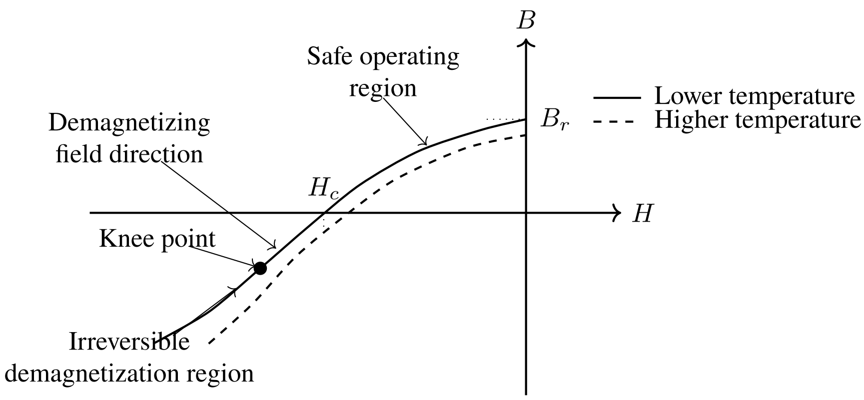

Figure 2.4: Simplified B-H demagnetization curve of a permanent magnet, showing the knee point, irreversible demagnetization region, and the effect of temperature on demagnetization resistance.

2.9.1 Magnetic Characteristics and Coercivity Limits

The resistance of a permanent magnet against demagnetization is mainly related to its coercivity. Coercivity shows how much reverse magnetic field the magnet can tolerate before its magnetic strength starts to decrease. This property is important in permanent magnet machines because the magnets may be exposed to demagnetizing fields during high-current operation or fault conditions.

The magnetic behavior of a permanent magnet can be described using the B-H characteristic curve. In the linear region, the magnet flux density can be written as

$$B_m = \mu_0 \mu_r H_m + B_r \tag{11}$$

where B_m is the magnet flux density, μ_0 is the permeability of free space, μ_r is the relative recoil permeability, H_m is the magnetic field strength inside the magnet, and B_r is the remanent flux density.

When a reverse magnetic field is applied, the operating point moves along the demagnetization curve. If the operating point remains above the knee point, the magnet can normally recover after the external field is removed. However, if the operating point is pushed below the knee point, irreversible demagnetization can occur.

The intrinsic coercivity H_{cj} is an important material property for evaluating this risk. A magnet with higher intrinsic coercivity can better resist demagnetizing fields. However, since coercivity decreases with increasing temperature, the magnet material and rotor geometry must be selected carefully to keep the magnet operating point in a safe region [15, 16].

2.10 Active Short-Circuit and Demagnetization Risk

In traction applications, Active Short-Circuit (ASC) is one of the important fault conditions that must be considered. During ASC, the inverter phases are short-circuited in a controlled way. This condition can produce large short-circuit currents in the stator windings.

These currents can create strong demagnetizing fields inside the rotor. If the demagnetizing field is high enough, it may push the magnet operating point below the knee point of the B-H curve and cause irreversible demagnetization. As a result, the motor may lose torque capability, resulting in degraded overall performance [17].

In this thesis, demagnetization is mainly evaluated under ASC conditions at elevated magnet temperatures. This is important because the studied heavy rare-earth-free magnet materials may have lower coercivity compared with stronger magnet grades. Therefore, the rotor topology, magnet arrangement, and machine configuration must be designed carefully to improve demagnetization robustness while maintaining the required torque performance.

2.11 Equivalent WLTP losses and Cost Evaluation

The Worldwide Harmonized Light Vehicles Test Procedure (WLTP) is a standard driving cycle used to evaluate the energy consumption and emission performance of light-duty vehicles. In electric vehicle applications, WLTP-based evaluation can provide useful information about how the traction motor performs under representative driving conditions. Since a traction motor does not operate at only one fixed torque-speed point, it is important to evaluate the machine over several operating regions.

In this thesis, selected torque-speed operating points are used to represent the most relevant operating regions of the WLTP driving condition. These points are not intended to reproduce the complete WLTP cycle. Instead, they are used to calculate an equivalent WLTP loss value, which provides a simplified loss-related comparison between the benchmark model and the redesigned candidate machines.

The equivalent WLTP loss is used to compare the overall loss behavior of different designs based on the selected operating points. A design with lower losses at these representative points can reduce the loss-related operating contribution and improve the overall vehicle-level performance.

Cost is another important factor in traction motor design. Permanent magnets can have a significant effect on the total material cost of an IPMSM, especially when rare-earth elements are used. Therefore, reducing the dependency on critical rare-earth materials is important not only for sustainability, but also for cost and supply-chain reasons.

In this work, the cost evaluation is mainly related to the selected magnet material, the amount of magnet used in each design, and the loss-related operating contribution represented by the equivalent WLTP loss. The redesigned candidates are compared with the benchmark model to investigate whether the required torque and efficiency can be maintained while using more cost-effective heavy rare-earth-free magnet materials. Therefore, the final design selection is based not only on electromagnetic performance and demagnetization robustness, but also on average losses, equivalent WLTP loss, and estimated material cost [7].

Chapter 3

Benchmark Model and Simulation Framework

This chapter describes the benchmark machine, the main design requirements, and the simulation framework used in this study. The studied benchmark machine is an Interior Permanent Magnet Synchronous Motor (IPMSM) and serves as the reference model for the redesign process. The aim of the redesign is to investigate whether the performance of the benchmark machine can be maintained, or further improved, by using weaker and more cost-efficient heavy rare-earth-free permanent magnet materials. Since these magnets may have different magnetic properties and demagnetization behavior, the redesign focuses on rotor topology, machine configuration, and selected geometrical parameters. The following sections describe the application requirements, benchmark configuration, material definition, simulation framework, and mesh strategy used in the analysis.

3.1 Application Context and Performance Requirements

The performance requirements used in this study were defined to represent the main operating demands of an electric vehicle traction motor. These requirements include torque capability, speed range, voltage and current limits, current density, airgap length, and packaging constraints. The requirements were used as fixed boundary conditions during the redesign process. Each redesigned candidate had to satisfy the same general operating and packaging limits before being considered for further evaluation. In addition, irreversible demagnetization during normal operation was not allowed, and torque degradation under severe operating or fault conditions had to remain within an acceptable range. These constraints provide a common basis for comparing the benchmark model with the redesigned candidates.

3.2 Benchmark Motor Configuration

The studied IPMSM was used as the reference model for the redesign process. It defines the initial machine layout before any design modifications are applied and provides the baseline for evaluating the redesigned candidates. The benchmark machine is an IPMSM designed for traction operation. It uses a predefined stator and rotor geometry together with a fixed electromagnetic and thermal design framework. The reference model also uses the N42UH permanent magnet material as the reference magnet material in the initial design. Since the main operating requirements and design constraints were already introduced in the previous section, this section focuses on the role of the benchmark model in the redesign process. The benchmark configuration is used as the comparison basis for evaluating the effect of alternative magnet materials, rotor topologies, and machine configurations. In the following chapters, the redesigned candidates are compared with this benchmark configuration to investigate whether the required performance can be maintained while improving selected design aspects such as demagnetization robustness, efficiency, weight, and estimated cost.

3.2.1 Stator and Winding Configuration

The stator configuration is an important part of the electromagnetic design because it affects the current distribution, magnetic loading, copper area, and available space for the rotor. In the benchmark model, the stator geometry is used as the initial reference for the redesign process. The benchmark stator uses a hairpin winding structure with rectangular slots. Hairpin windings are suitable for traction applications because they provide high current capability, compact packaging, and good thermal behavior. In this study, the general stator layout was kept as a reference, while selected stator-related parameters were considered during the redesign and optimization process. The main stator and winding parameters considered in this work include the stator dimensions, slot geometry, hairpin conductor dimensions, conductor positioning, and cooling-related geometrical features. These parameters influence the electromagnetic loading, current density, local saturation, and winding space available in the machine. Table 3.1 summarizes the stator and winding parameter groups considered in the study.

Table 3.1: General stator and winding parameter groups considered in the study

Parameter group	**Related design aspects**
Stator dimensions	Inner and outer stator dimensions
Slot geometry	Slot height, slot width, and slot opening
Hairpin winding	Number of slots, hairpin layers, and conductor dimensions
Conductor positioning	Pin position and spacing inside the slot
Cooling-related geometry	Cooling channel dimensions and position

The main stator and winding parameter groups listed in Table 3.1 are illustrated in Figure 3.1. The figure provides a simplified view of the key slot and conductor-related dimensions considered during the redesign process.

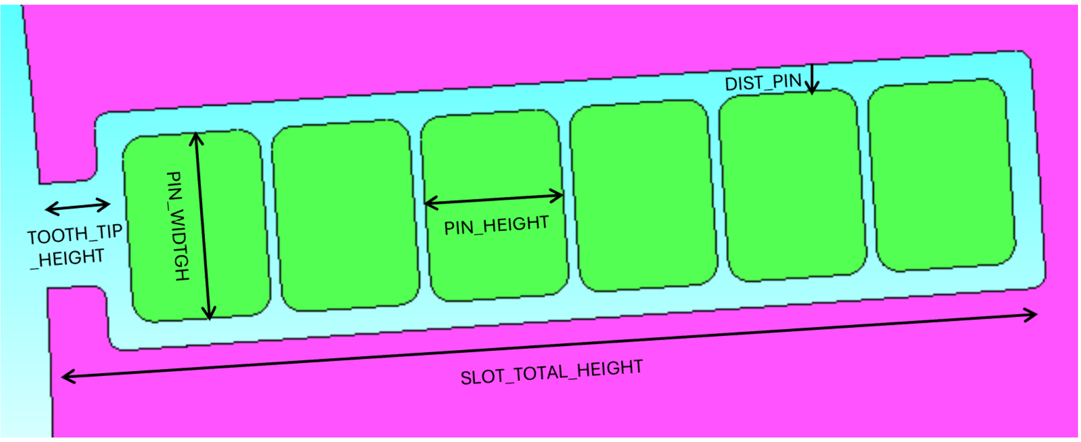

Figure 3.1: Simplified illustration of the main stator slot and winding parameters considered during the redesign process.

These parameters are important because they define the available winding space and influence the electromagnetic and thermal behavior of the stator.

3.2.2 Rotor Geometry and Magnet Definition

The rotor is one of the main parts of the redesign process in this study, since the rotor geometry directly affects the magnetic flux path, saliency, torque production, and magnet exposure to demagnetizing fields. The benchmark rotor was used as the initial reference geometry before applying any topology or geometrical modifications.

The main rotor-related parameters considered in the redesign include the rotor dimensions, magnet position, magnet height, magnet depth, bridge thickness, magnet spacing, and magnet angles. These parameters influence the electromagnetic performance of the machine and also affect the demagnetization behavior of the permanent magnets under severe operating conditions.

The reference model uses the N42UH permanent magnet material as the initial magnet definition. In the redesign study, alternative heavy rare-earth-free magnet materials were also investigated together with different rotor topologies in order to evaluate their effect on torque capability, efficiency, cost, and demagnetization robustness.Table 3.2 summarizes the rotor and magnet parameter groups considered in the study.

Table 3.2: General rotor and magnet parameter groups considered in the study

Parameter group	**Related design aspects**
Rotor dimensions	Inner and outer rotor geometry
Magnet geometry	Magnet height, depth, and width
Magnet position	Magnet placement inside the rotor
Bridge geometry	Central and outer bridge regions
Magnet spacing	Distance between magnet sections
Magnet angle	Inner and outer magnet orientation
Magnet material	Reference and alternative magnet grades

The rotor and magnet parameter groups listed in Table 3.2 are also illustrated in Figure 3.2. The figure provides a simplified view of the main magnet-related geometrical features considered during the redesign process.

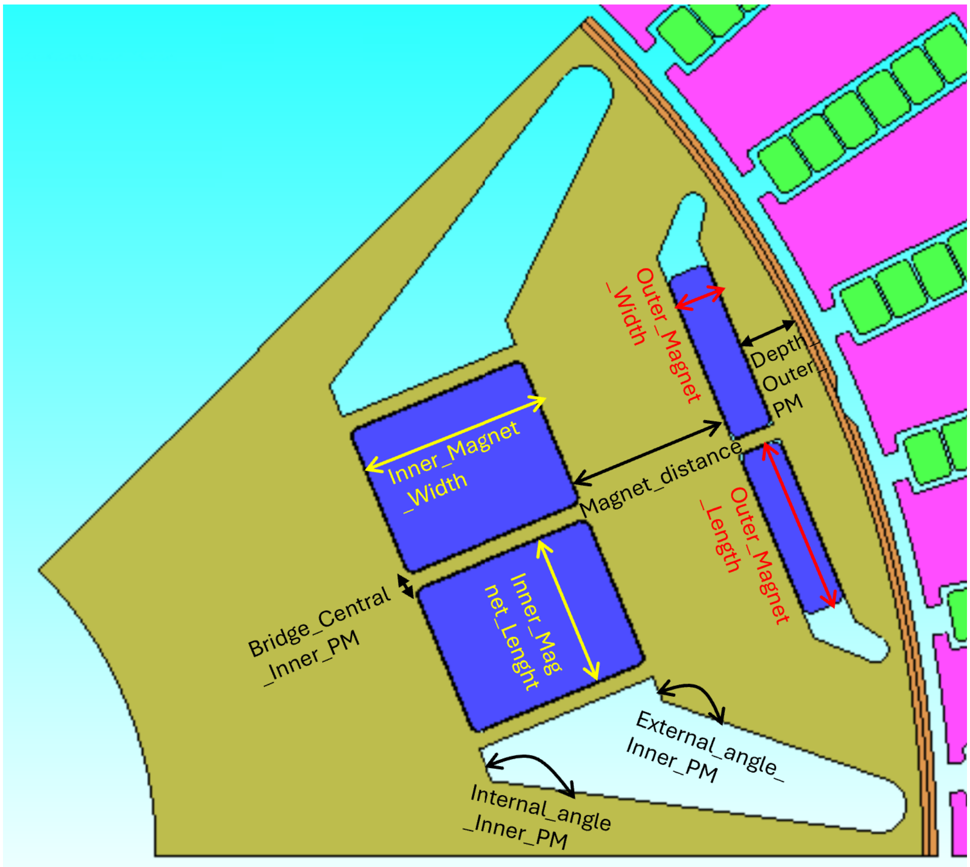

Figure 3.2: Simplified illustration of the main rotor and magnet parameters considered during the redesign process.

These rotor and magnet parameters are important because they define the flux path inside the rotor and influence the balance between torque capability and demagnetization robustness.

3.2.3 Benchmark Material Definition

The electromagnetic model requires material definitions for the main components of the benchmark machine, including the winding, stator core, rotor core, and permanent magnets. In the benchmark model, copper is used for the winding, electrical steel is used for the stator and rotor cores, and N42UH is used as the reference permanent magnet material. The material properties directly affect the flux distribution, torque capability, iron losses, and demagnetization behavior of the machine. In particular, the B-H characteristics of the permanent magnet are important for evaluating its response under demagnetizing fields and elevated temperature conditions. The B-H curve of the N42UH magnet used in the benchmark model is shown in Figure 3.3.

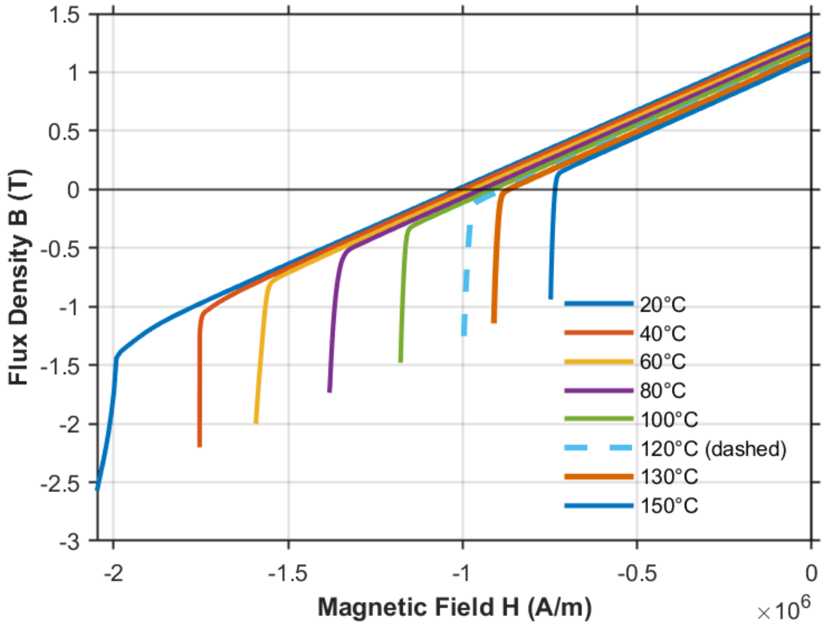

Figure 3.3: B-H characteristics of the N42UH benchmark magnet material.

The main material definitions used in the benchmark model are summarized in Table 3.3.

Table 3.3: Main material definitions used in the benchmark model

Part	**Material**
Winding	Copper
Permanent magnet	N42UH
Stator and rotor core	Electrical steel

This material definition was used as the benchmark reference before introducing the alternative magnet materials and redesigned rotor configurations in the following chapters.

3.3 Simulation Framework

The electromagnetic behavior of the machine was evaluated using finite element simulations in JMAG. The simulation model includes the stator, rotor, winding, permanent magnets, airgap, and the material properties required for electromagnetic analysis. A two-dimensional FEM model was used to calculate the main electromagnetic quantities of the machine. The simulation framework was used to evaluate torque capability, torque ripple, magnetic flux density distribution, efficiency-related operating points, and demagnetization behavior. Both normal operating conditions and Active Short-Circuit (ASC) fault conditions were considered in the study. Using the same simulation framework for the benchmark model and the redesigned candidates makes it possible to compare different design options in a consistent way. The detailed evaluation procedure, including topology screening, ASC assessment, and optimization steps, is presented in the methodology chapter. The main simulation setup used in this study is summarized in Table 3.4.

Table 3.4: Simulation setup used in this study

Item	Description
Software	JMAG
Simulation method	Finite Element Method (FEM)
Model type	Two-dimensional electromagnetic model
Machine type	Interior Permanent Magnet Synchronous Motor
Control strategy	MTPA
Normal operation evaluation	Torque, flux density, and efficiency-related points
Fault condition evaluation	Active Short-Circuit (ASC)
Demagnetization evaluation	Magnet robustness under demagnetizing field

3.4 Mesh Definition

The finite element mesh was defined in JMAG using a sliding mesh approach for the rotating machine model. This method allows the rotor motion to be represented while keeping a controlled mesh connection across the airgap region. Automatic element sizing was used as the general meshing method, while additional attention was given to regions where high magnetic field variation was expected. A finer mesh was applied close to the airgap, magnet edges, flux barriers, and slot openings. These regions are important because the magnetic flux changes rapidly there, and inaccurate meshing may directly affect the calculated torque, flux density distribution, and demagnetization results. The mesh around the air barriers and magnet corner points was refined to better represent the sharp geometrical transitions. Similarly, the stator slot regions close to the airgap were meshed with higher detail because this part strongly influences local saturation, MMF distribution, and torque ripple behavior. Figure 3.4 shows the generated mesh used for the benchmark model.

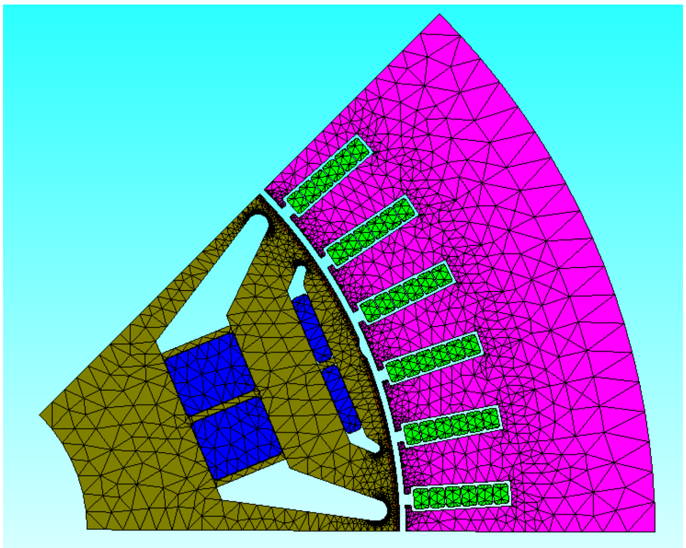

Figure 3.4: Generated finite element mesh for the benchmark machine model using local refinement in critical electromagnetic regions.

This mesh strategy was used to keep the simulation accurate in the critical electromagnetic regions while avoiding an unnecessary increase in the total number of elements. In this way, the model could still be solved efficiently, while the main torque and demagnetization-related results remained reliable.

Chapter 4

Evaluation Methodology and Operating Scenarios

4.1 Benchmark Model and Design Objective

This chapter describes the evaluation methodology used to compare the benchmark model and the redesigned candidate machines. The methodology was based on a step-by-step process, starting from magnet material comparison and rotor topology screening, followed by machine configuration screening, ASC demagnetization evaluation, candidate selection, and optimization. The purpose of this approach was to reduce the design space gradually and identify suitable candidate models for further optimization. All candidate designs were evaluated using the same simulation framework in JMAG in order to make the comparison consistent.

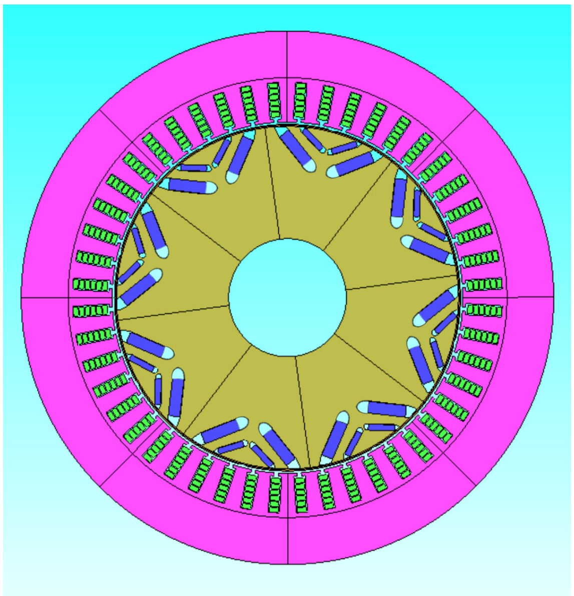

Figure 4.1: Investigated rotor topologies used for the initial topology screening.

4.2 Magnet Material Selection and Comparison Method

The first step of the study was to compare three permanent magnet materials: N42UH, F45H, and F48SH. The N42UH magnet was used as the reference magnet material, while F45H and F48SH were investigated as alternative candidate magnets for the redesigned machine configurations. Since the magnet material strongly affects both torque capability and demagnetization behavior, the B-H characteristics of the three magnets were compared under the same temperature condition, as shown in Figure 4.2. This comparison was used to understand the magnetic strength, coercivity level, and demagnetization sensitivity of each material. The comparison showed that F45H can support torque production and cost reduction due to its higher flux density capability. However, its lower coercivity makes it more sensitive to irreversible demagnetization under severe ASC conditions. In contrast, F48SH provides stronger demagnetization resistance and better magnetic robustness, while N42UH represents the reference behavior of the benchmark model. Therefore, the magnet comparison was based on the trade-off between torque capability, demagnetization robustness, and material cost. These observations were then used together with topology selection and parametric optimization in the following design stages.

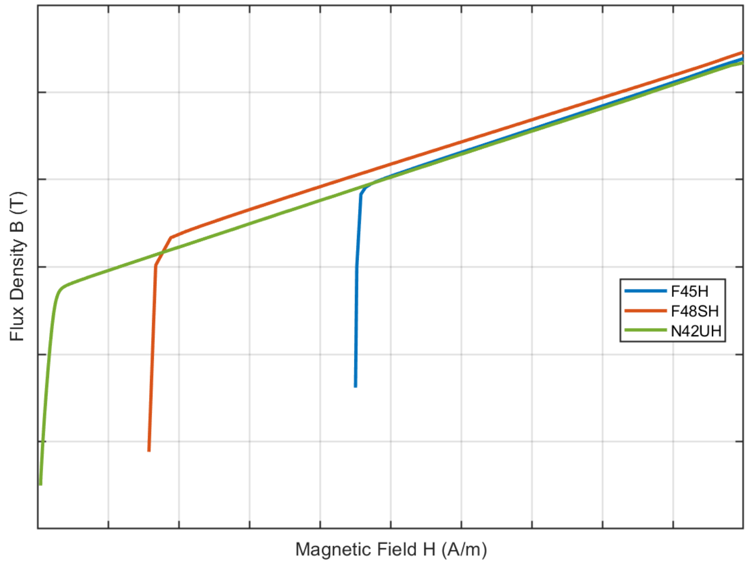

Figure 4.2: Comparison of the B-H characteristics for N42UH, F45H, and F48SH magnets.

4.3 Rotor Topology Screening Method

After the magnet comparison, different rotor topologies were investigated to evaluate how the magnet arrangement inside the rotor affects the flux path, torque capability, and demagnetization behavior under ASC conditions. The investigated topologies included U, UU, V, VV, UI, VI, and UI*, as shown in Figure 4.3. The selected topologies were designed to represent different flux barrier structures and magnet segmentation concepts. The V and VV configurations were used to study single-layer and double-layer V-shaped arrangements, while the U and UU topologies were investigated to evaluate the influence of U-shaped flux barriers and magnetic shielding behavior. In addition, the UI and VI structures introduced an extra I-shaped magnet section to improve flux guidance and rotor space utilization. The UI* topology was considered as a modified segmented version of the UI structure. In this topology, the magnet arrangement was divided into smaller sections in order to improve flux distribution and reduce local demagnetization sensitivity. At this stage, the objective was to define and compare the main rotor design alternatives before moving to detailed ASC analysis and parametric optimization. The quantitative comparison of the investigated topologies is presented in the results chapter.

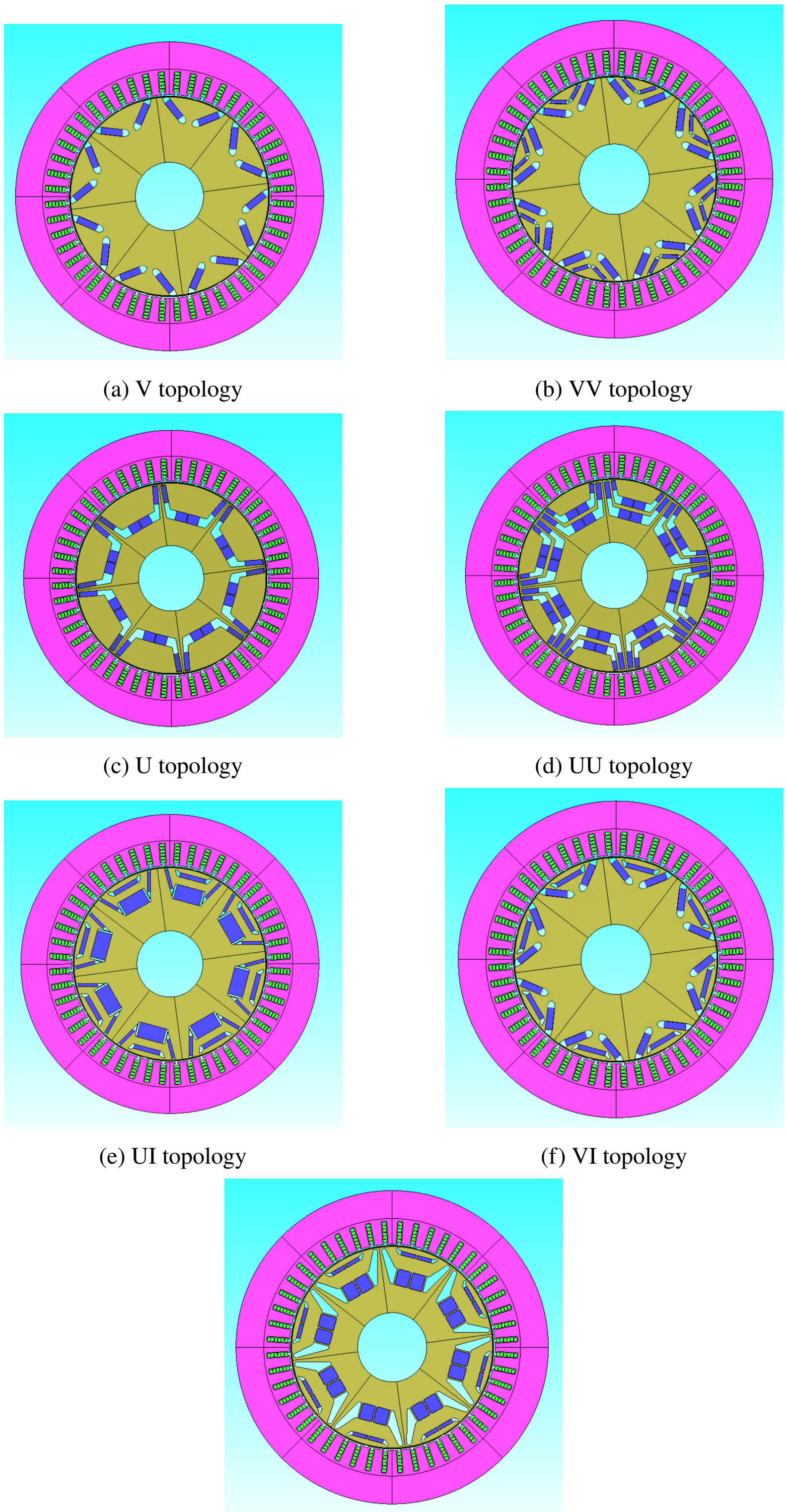

(a) V topology
(b) VV topology
(c) U topology
(d) UU topology
(e) UI topology
(f) VI topology
(g) UI* topology

Figure 4.3: Investigated rotor topologies used for the screening study, including V, VV, U, UU, UI, VI, and UI* configurations.

4.4 Machine Configuration Screening

In the next step, different machine configurations were considered based on the number of poles, stator slots, and hairpin layers. In the notation used in this work, P represents the number of poles, H represents the number of hairpin layers, and S represents the number of stator slots. For example, 8P-6H-48S represents a machine with 8 poles, 6 hairpin layers, and 48 stator slots. Several configurations were included in the initial screening in order to study the influence of the main machine layout on torque capability, MMF distribution, current loading, and demagnetization behavior. Figure 4.4 summarizes the main design parameters and configuration options evaluated during the screening process.

Design Parameter	Options Evaluated
Pole Number (P)	6 8
Slot Configuration (S)	48 54 72
Hairpin Layers	6 8

Figure 4.4: Design parameters and machine configuration options considered during the initial screening process.

The purpose of this screening stage was to define the design space and identify suitable candidate configurations for the following ASC and topology investigations. At this stage, the focus was mainly on comparing the machine layouts rather than presenting final optimized results.

4.5 ASC Demagnetization Evaluation Method

After the initial configuration screening, the rotor topologies were evaluated under Active Short-Circuit (ASC) conditions. ASC was included because it represents one of the most critical fault conditions in electric vehicle traction motors and can expose the permanent magnets to strong demagnetizing fields.

In this study, the ASC condition was implemented in JMAG using an external circuit model with controlled switches, as shown in Figure 4.5. The three phase terminals of the machine were connected to the external circuit, and the switching sequence was used to change the machine operation from normal operation to short-circuit operation during the simulation.

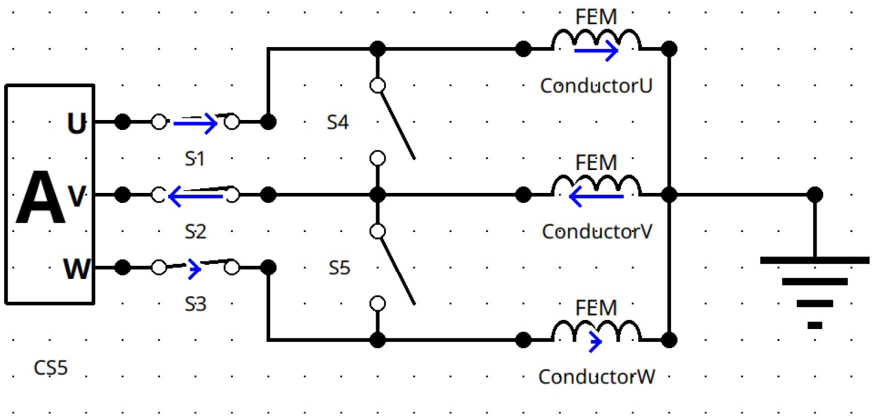

Figure 4.5: External JMAG circuit used to implement the ASC event through controlled switches and three-phase short-circuit connections.

In contrast to the simplified ASC schematic, the JMAG circuit includes the controlled switches and phase connections used to reproduce the short-circuit event during the transient simulation. Switches S1, S2, and S3 were connected to the three phase terminals of the machine and followed the defined switching sequence. In the initial state, these switches were ON. At the first transition point, corresponding to step 120, S1, S2, and S3 were turned OFF. At the second transition point, corresponding to step 360, they were turned ON again. The total switching period was defined as 481 steps.

Switches S4 and S5 were controlled in the opposite state compared with S1, S2, and S3. Therefore, when S1, S2, and S3 were turned OFF, S4 and S5 were turned ON to create the short-circuit path between the machine phase terminals. This switching arrangement allowed the ASC event to be applied during the selected time interval of the simulation.

The ASC evaluation was performed for the candidate magnet materials at elevated magnet temperatures. The maximum magnet temperature was set to 130°C, which represents the worst-case magnet condition considered in this study. This temperature is critical because permanent magnets become weaker at elevated temperatures, and their resistance against demagnetizing fields decreases.

The main comparison criterion used in this stage was the torque reduction after the fault condition. This value was used as an indicator of irreversible demagnetization, magnet robustness, and topology sensitivity. The detailed torque reduction results and demagnetization maps are presented in the results chapter.

4.6 Selection of Candidate Models for Optimization

Based on the topology screening and ASC evaluation, the most promising rotor topology and magnet combination were selected for further investigation. The selection process considered the balance between torque capability, demagnetization robustness, and cost-oriented design requirements.

After the initial topology selection, the chosen rotor structure and magnet material were evaluated in several machine configurations. Different slot numbers, hairpin layers, and parallel path arrangements were investigated to study their influence on current distribution, torque capability, and ASC fault behavior.

Based on this comparison, two candidate configurations were selected for the next optimization stage: one torque-oriented candidate and one robustness-oriented candidate. The torque-oriented candidate was selected because it showed strong baseline electromagnetic performance, while the robustness-oriented candidate was selected because it showed improved demagnetization behavior under ASC conditions.

4.7 Parametric Optimization

After selecting the two candidate configurations, a parametric optimization study was performed to investigate the effect of the main geometrical parameters on the electromagnetic performance of the machine. The objective of this stage was to understand how each parameter affects torque capability, magnetic loading, flux distribution, current density, and demagnetization robustness before applying the automatic genetic algorithm-based optimization process.

On the stator side, the investigated parameters were mainly related to the airgap, slot geometry, conductor dimensions, conductor position, and active stack length. These parameters affect the available copper area, current density, magnetic saturation in the stator teeth, airgap flux density, and the total active volume of the machine.

On the rotor and magnet side, the investigated parameters were mainly related to the rotor outer diameter, magnet dimensions, magnet angles, and magnet depths. These parameters affect the internal flux path, flux concentration, saliency, magnet utilization, and the exposure of the magnets to demagnetizing fields during ASC operation.

Some parameters have similar physical effects and were therefore grouped together in the tables. For example, pin width and pin height both influence the conductor cross-sectional area and current carrying capability. Similarly, inner and outer magnet dimensions both affect magnet volume, flux contribution, and local saturation. The main parameters considered during the parametric optimization are summarized in Tables 4.1 and 4.2.

Table 4.1: Main stator parameters considered during manual parametric optimization

Parameter	**Effect of parameter variation**
Pin width and pin height	Change conductor cross-sectional area, current capability, and slot filling factor.
Airgap size	Affects magnetic coupling, airgap flux density, leakage flux, and torque production.
Stack length	Changes active machine volume, torque capability, weight, and material usage.

Table 4.2: Main rotor and magnet parameters considered during manual parametric optimization

Parameter	**Effect of parameter variation**
Rotor outer diameter	Changes rotor radius, airgap flux density, electromagnetic loading, and torque capability.
Outer and inner magnet length/width	Change magnet volume, flux contribution, torque capability, saturation, and material cost.
Outer and inner magnet angle	Affect flux direction, internal flux path, saliency, leakage flux, and airgap coupling.
Outer magnet depth	Changes the outer magnet position and its exposure to demagnetizing fields.
Inner magnet depth	Affects internal flux path, leakage flux, magnet shielding, and ASC robustness.

During this stage, the parameters were varied within the defined design limits. Their effects on torque, flux distribution, saturation, and demagnetization behavior were evaluated.

4.8 Genetic-Algorithm based Optimization and Final Evaluation Criteria

After the parametric optimization, the two selected candidate configurations were further optimized using JMAG FEA enviroment. The purpose of this stage was to improve the designs in a more systematic way and to find a better balance between torque performance and demagnetization robustness.

The optimization process was defined based on several objectives. These objectives included maintaining the required torque capability, reducing torque degradation under ASC, improving magnetic flux distribution, reducing critical demagnetization regions, and keeping the design practical in terms of geometry and machine constraints.

After optimization, the final candidate models were compared with the benchmark model. This comparison was based on peak torque, demagnetization robustness under ASC, motor weight, estimated cost, and efficiency at selected torque-speed operating points.

For the efficiency evaluation, the final models and the benchmark model were assessed at five selected torque-speed operating points. These points were chosen to represent the most relevant operating regions of the WLTC driving cycle, as summarized in Table 4.3.

Table 4.3: Selected torque-speed operating points for efficiency evaluation

Operating point	Torque (Nm)	Speed (rpm)
Point A	25	1092
Point B	6	3641
Point C	23	3641
Point D	20	5721
Point E	30	8731

4.9 Candidate Selection and Post-Processing Procedure

The optimization process generated a large number of candidate designs for each investigated machine configuration. For every selected machine layout and magnet combination, more than 500 design candidates were produced by the Genetic Algorithm optimization module through variations of the selected design parameters within their predefined limits.

The best 5 candidates which proves the balances for all constraint and requirements were selected from the optimization. The optimization results were exported from Genetic Algorithm and further processed using MATLAB. The post-processing stage was used to compare the generated candidates based on several performance indicators simultaneously rather than relying on a single objective value.

The candidate selection process considered average torque, total losses, efficiency at the selected operating points, demagnetization behavior, torque degradation after ASC operation, and estimated material cost. Since these performance indicators often show conflicting trends, a trade-off analysis was performed to identify solutions that provide a balanced overall performance.

The candidate filtering process was carried out in multiple stages. The candidates were then ranked according to their loss behavior, efficiency performance, demagnetization robustness, and material usage. Finally, a limited number of designs were selected for detailed verification.

Figure 4.6 illustrates the overall candidate selection and post-processing procedure used in this work.

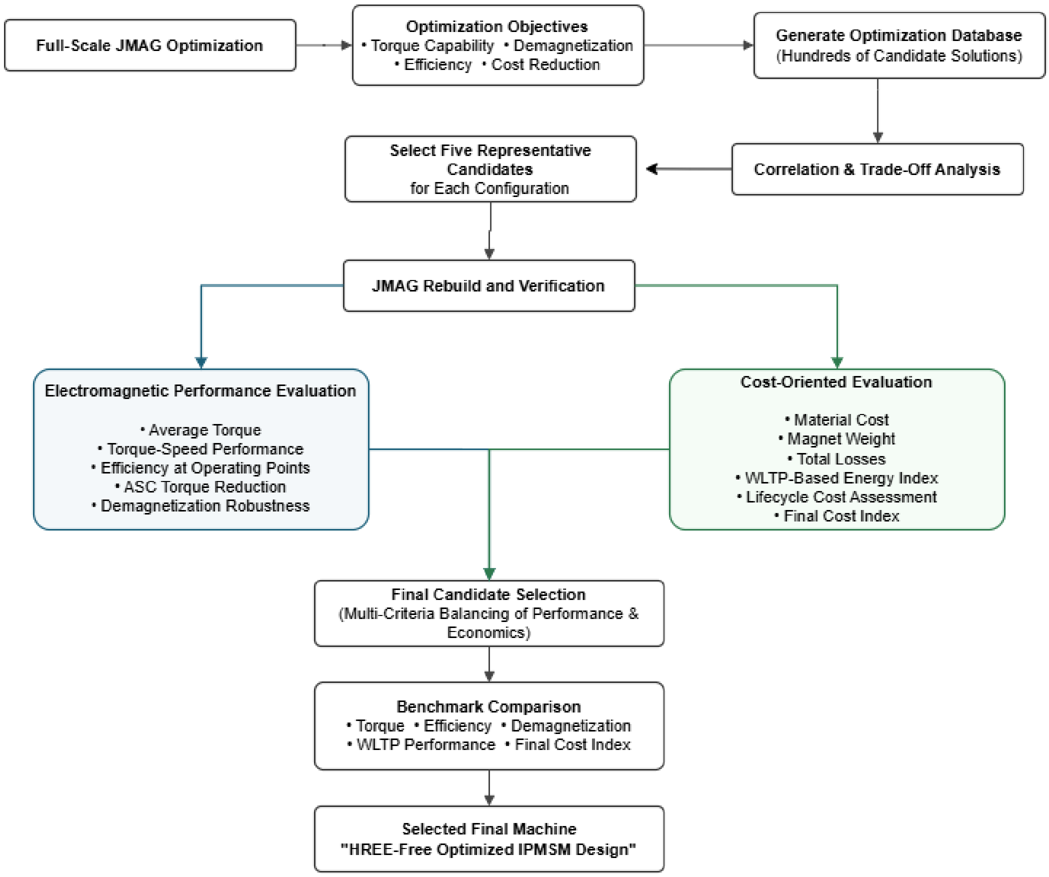

Figure 4.6: Candidate selection workflow used the Genetic Algorithm optimization process

The selected candidates were subsequently rebuilt and re-simulated in JMAG in order to verify the optimization results and to provide a consistent basis for the final comparison with the benchmark machine. The detailed performance comparison of the selected candidates is presented in Chapter 6.

Chapter 5

Topology Screening and Preliminary Parametric Optimization

This chapter presents the simulation results obtained from the topology screening and preliminary parametric optimization stages. Different rotor topologies and machine configurations were evaluated under identical operating conditions in order to compare their electromagnetic performance and ASC robustness.

Based on the obtained results, two candidate configurations were selected for further investigation according to their balance between torque capability, flux distribution, and demagnetization behavior. Preliminary geometrical modifications were then applied to improve the overall electromagnetic performance before proceeding to the full-scale optimization stage presented in the next chapter.

5.1 Topology Screening and Rotor Geometry Selection

The investigated rotor topologies and machine configurations were evaluated under ASC operating conditions using finite element simulations in JMAG. The comparison focused mainly on torque capability, flux distribution behavior, and torque reduction after the fault condition.

The obtained results showed clear differences between the investigated structures in terms of demagnetization robustness and electromagnetic loading. Among the evaluated candidates, the UI* topology provided the most balanced behavior between torque capability and ASC robustness.

After the topology evaluation, different pole-slot and hairpin combinations were also compared. Based on the preliminary simulation results, the 8P-6H-48S configuration showed the most suitable balance between electromagnetic performance and fault robustness and was therefore selected as the main reference configuration for the following analyses.

The next sections present the detailed comparative results and the preliminary optimization study of the selected candidate configurations.

5.1.1 Topology Comparison Under ASC Condition

After selecting the 8P-6H-48S configuration, the investigated rotor topologies were compared under Active Short-Circuit (ASC) operation in order to evaluate their robustness against irreversible demagnetization. In this study, the maximum magnet temperature was set to 130°C, which represents the worst-case operating condition considered for the magnet. This temperature is critical because permanent magnets become weaker at elevated temperatures, and their resistance against demagnetizing fields is reduced. Therefore, the ASC evaluation at 130°C was used as the main worst-case condition for comparing the demagnetization robustness of the different topologies.

In addition to the 130°C case, the topologies were also evaluated at 120°C to observe the temperature effect on torque reduction. Tables 5.1 and 5.2 summarize the torque reduction results for all investigated topologies at 120°C and 130°C, respectively, using both F48SH and F45H magnet materials.

The results show that the weaker magnet material, F45H, leads to significantly higher torque reduction in all investigated topologies compared with F48SH. This is mainly because F45H has lower coercivity and is therefore more sensitive to irreversible demagnetization under severe ASC conditions, especially at the maximum magnet temperature of 130°C.

Among all investigated rotor geometries, the UI* topology showed the lowest torque reduction for both magnet materials and both temperature levels. This indicates that the UI* topology provides better protection for the magnets against demagnetizing fields during ASC operation. In contrast, the U and UU topologies showed larger torque degradation, which can be related to less favorable flux paths and higher magnet exposure to demagnetizing fields.

The V, VV, UI, and VI topologies showed a more balanced behavior between torque capability and ASC robustness. However, based on the torque reduction results, the UI* topology was selected as the most promising topology for further investigation and optimization.

Table 5.1: Torque reduction comparison under ASC operation at 120°C.

Topology	**F48SH (%)**	**F45H (%)**
V	5.98	29.89
VV	1.88	25.70
U	6.93	34.34
UU	3.66	33.60
UI	3.27	26.05
VI	5.15	28.47
UI*	0.37	8.75

Table 5.2: Torque reduction comparison under ASC operation at 130°C.

Topology	**F48SH (%)**	**F45H (%)**
V	7.59	32.55
VV	6.15	32.02
U	14.91	36.97
UU	9.82	39.84
UI	7.88	30.07
VI	10.46	35.29
UI*	1.59	11.54

Although Tables 5.1 and 5.2 summarize the overall torque reduction after ASC operation, the local demagnetization distribution inside the magnets is also important for understanding the robustness of each topology. Therefore, the demagnetization contour of the selected UI* topology is shown for both F45H and F48SH magnet materials.

Figures 5.1a and 5.1b show the demagnetization ratio distribution of the UI* topology under ASC condition at elevated magnet temperature. The comparison shows how the magnet material affects the local demagnetization behavior, with the same rotor topology.

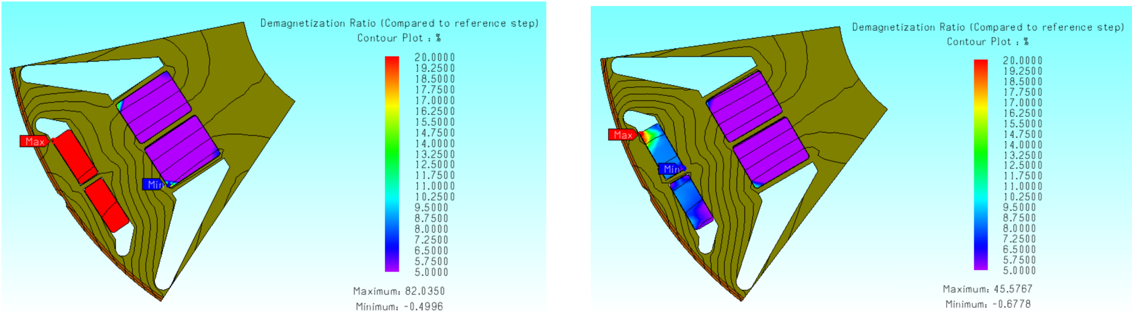

(a) F45H magnet material

(b) F48SH magnet material

Figure 5.1: Demagnetization ratio distribution of the UI* topology under ASC condition for F45H and F48SH magnet materials.

The contour plots support the torque reduction results by showing that the UI* topology limits the critical demagnetization regions compared with other topologies. However, the F45H magnet shows higher local demagnetization sensitivity than F48SH, which is consistent with the larger torque reduction reported in the tables.

5.1.2 Comparison of Different Pole, Slot, and Hairpin Configurations

In addition to the selected 8P-6H-48S configuration, several other machine configurations were investigated in order to evaluate the influence of pole number, slot number, and hairpin layers on the ASC performance. Figures 5.2, 5.3, 5.4, and 5.5 present the torque reduction comparison at 130°C for different topology groups under ASC operation.

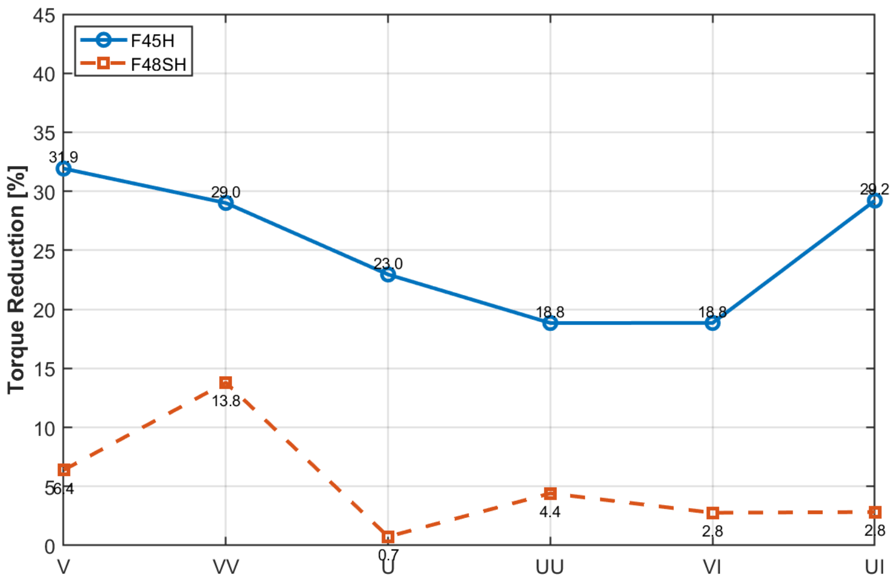

Figure 5.2: Torque reduction comparison for the 6P-6H-54S configuration under ASC operation at 130°C.

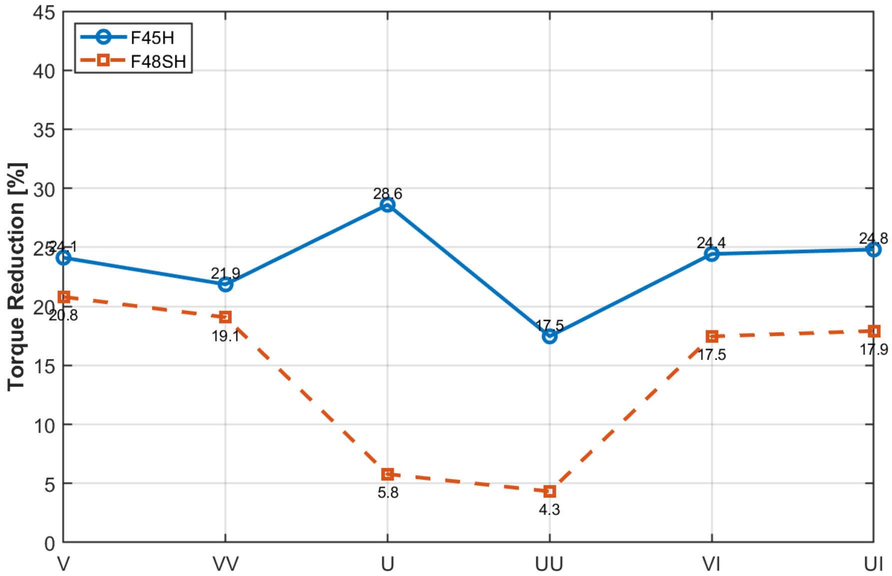

Figure 5.3: Torque reduction comparison for the 6P-8H-54S configuration under ASC operation at 130°C.

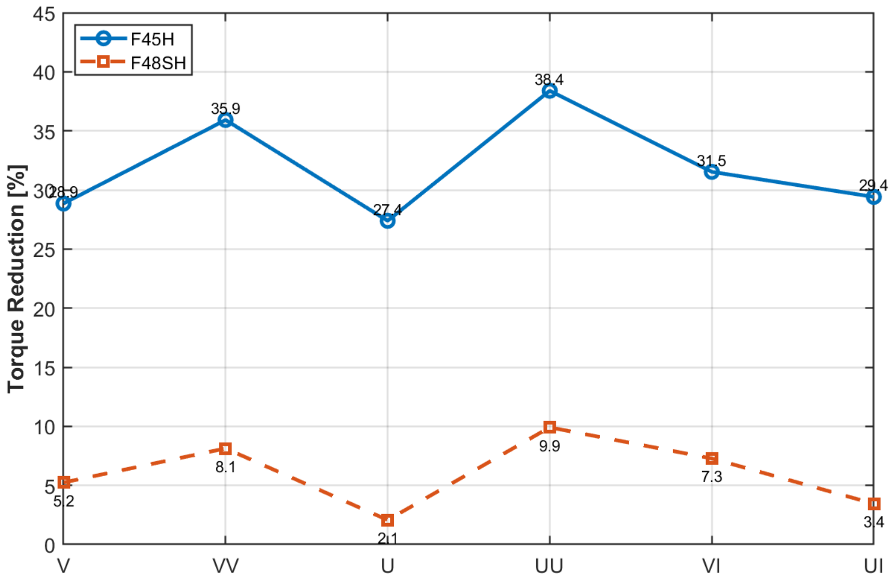

Figure 5.4: Torque reduction comparison for the 8P-6H-48S configuration under ASC operation at 130°C.

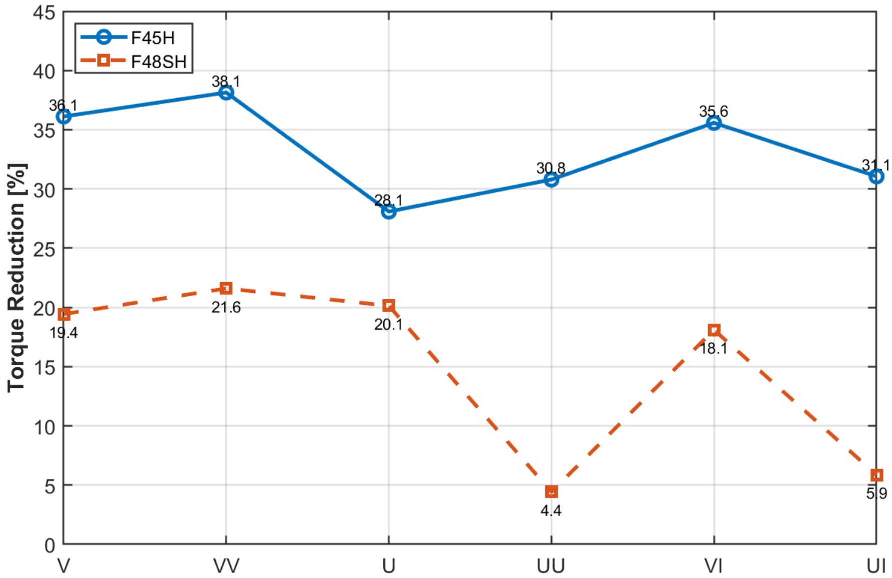

Figure 5.5: Torque reduction comparison for the 8P-8H-48S configuration under ASC operation at 130°C.

As shown in Figures 5.2–5.5, the F45H magnet generally resulted in higher torque reduction compared to the F48SH magnet for all investigated configurations. This behavior confirms that weaker HREE-free magnets are more sensitive to irreversible demagnetization under severe ASC conditions.

The results also indicate that the pole number, slot configuration, and hairpin arrangement strongly influence the demagnetization robustness of the machine. Configurations with higher magnetic loading and larger current concentration generally experienced higher torque degradation during the fault condition.

Among the investigated configurations, the previously selected 8P-6H-48S geometry still provided the most balanced behavior between torque capability and ASC robustness. Therefore, this configuration was selected as the main candidate for the next stages of parametric optimization and detailed analysis.

5.1.3 F45H Configuration Selection and Parallel Path Evaluation

After comparing the F45H and F48SH magnet grades, the F45H magnet was selected for the next stage due to its lower material cost and reduced dependency on heavy rare-earth elements. Although F48SH showed better resistance against demagnetization, the main purpose here was to investigate whether the weaker F45H magnet could still provide acceptable performance through topology and configuration improvement.

Three UI* configurations were selected for further evaluation, as shown in Figure 5.6. These configurations were chosen to study the effect of increasing the slot number, increasing the number of hairpin layers, and changing the parallel path arrangement under ASC condition.

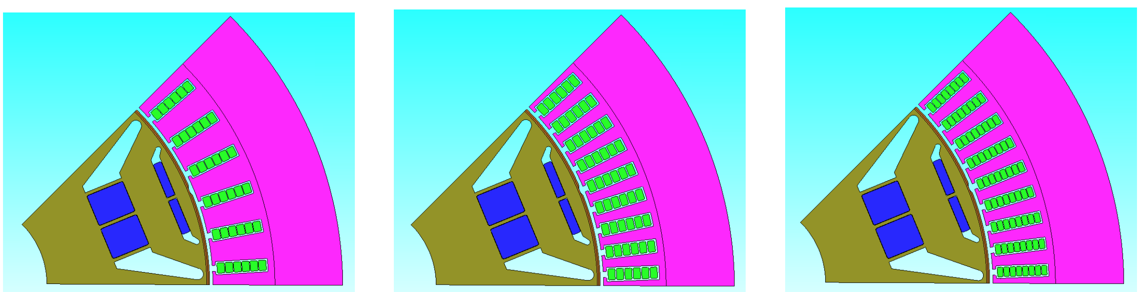

(a) 8P-6H-48S (b) 8P-6H-72S (c) 8P-8H-72S

Figure 5.6: Selected UI* configurations investigated with the F45H magnet.

The first evaluated configuration was the 8P-6H-48S model with two parallel paths. As shown in Figure 5.7, this design provides relatively high torque before ASC, but the torque reduction is still high. This indicates that the baseline configuration has good torque capability, but it is more sensitive to demagnetization under fault condition.

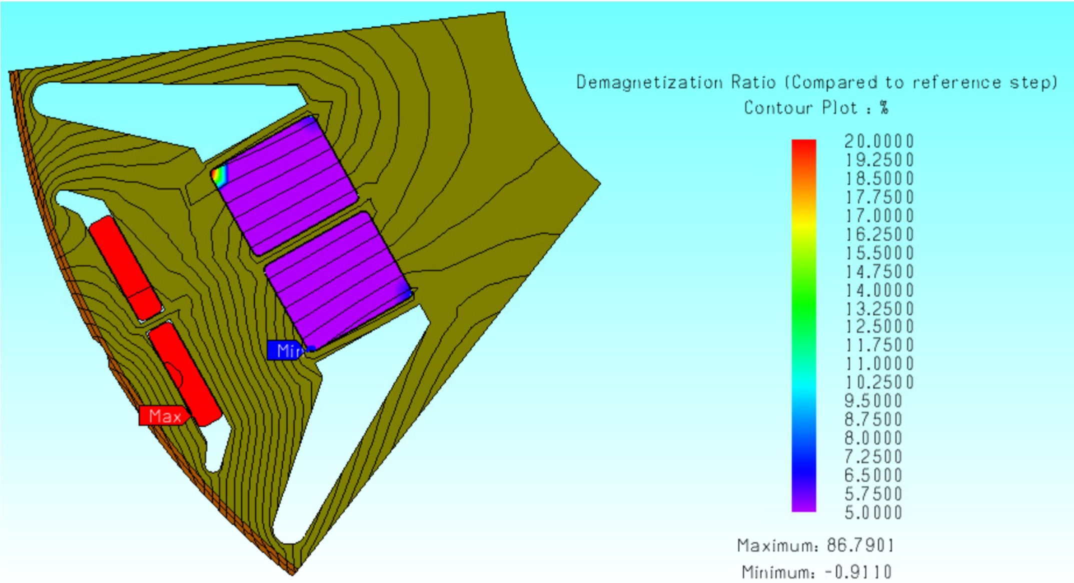

Figure 5.7: Demagnetization result for the UI* 8P-6H-48S configuration under ASC operation at 130°C using F45H.

Table 5.3: Performance summary of the UI* 8P-6H-48S configuration under ASC operation at 130°C using F45H.

Parallel Path	Torque before ASC (p.u.)	Torque after ASC (p.u.)	Torque Reduction (%)
2PP	0.956	0.824	13.73

To improve the electromagnetic distribution, the slot number was increased from 48 to 72 while keeping the same 6-layer hairpin arrangement. The comparison in Figure 5.8 and Table 5.4 shows that the 2PP case gives a much lower torque reduction than the 48-slot configuration. However, the 3PP case gives higher torque before ASC but also higher torque reduction, showing that the parallel path selection has a strong influence on fault robustness.

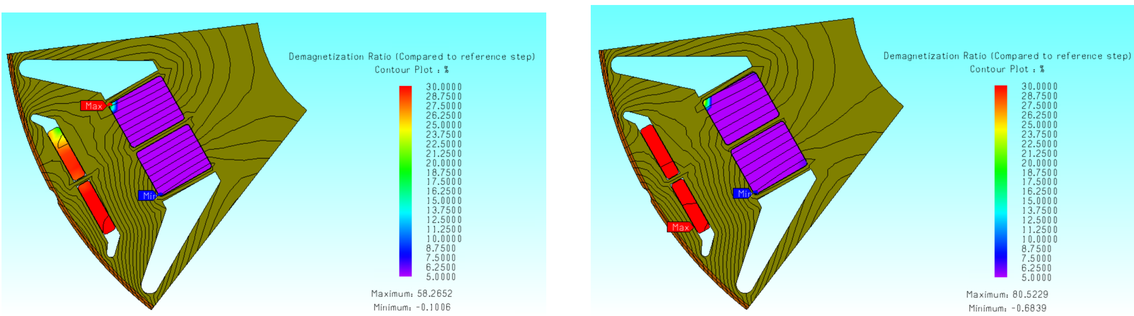

(a) 2PP

(b) 3PP

Figure 5.8: Demagnetization comparison for the UI* 8P-6H-72S configuration under ASC operation at 130°C using F45H.

Table 5.4: Performance summary of the UI* 8P-6H-72S configuration under ASC operation at 130°C using F45H.

Parallel Path	**Torque before ASC (p.u.)**	**Torque after ASC (p.u.)**	**Torque Reduction (%)**
2PP	0.750	0.709	5.44
3PP	0.912	0.811	11.08

In the final configuration, the number of hairpin layers was increased from 6 to 8 while keeping the 72-slot stator. As shown in Figure 5.9, the demagnetization behavior becomes more stable for both parallel path options. The results in Table 5.5 show that both 2PP and 3PP cases have torque reduction close to 6%, which means that this configuration is less sensitive to the parallel path arrangement.

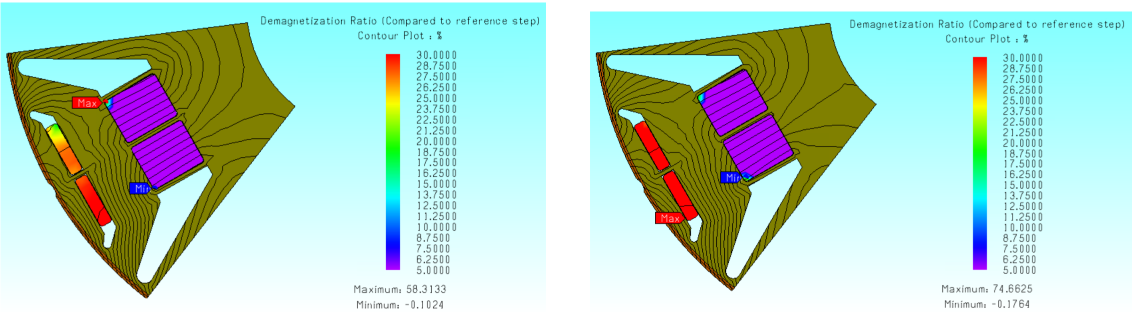

(a) 2PP (b) 3PP

Figure 5.9: Demagnetization comparison for the UI* 8P-8H-72S configuration under ASC operation at 130°C using F45H.

Table 5.5: Performance summary of the UI* 8P-8H-72S configuration under ASC operation at 130°C using F45H.

Parallel Path	**Torque before ASC (p.u.)**	**Torque after ASC (p.u.)**	**Torque Reduction (%)**
2PP	0.825	0.773	6.33
3PP	0.911	0.855	6.15

Overall, increasing the slot number from 48 to 72 clearly improves the ASC robustness, especially for the 2PP case. Increasing the hairpin layers from 6 to 8 gives a more balanced result, where both parallel path options show similar torque reduction. Therefore, the 8P-6H-48S model remains useful as a high-torque baseline, while the 8P-8H-72S configuration shows better robustness and a more stable response under ASC operation.

5.2 Candidate Model Selection for Preliminary Optimization

Based on the topology and configuration screening results, two UI* configurations were selected for further optimization. The selection was not based only on the highest torque value, but also on the torque reduction after ASC and the overall robustness of the machine under fault conditions. This was important because the selected F45H magnet is more cost-effective, but also more sensitive to irreversible demagnetization compared with F48SH.

The evaluated configurations showed different design strengths. Some cases provided higher average torque before ASC, while others showed lower torque degradation after ASC. Therefore, the purpose of this stage was to select two representative models that could define two different optimization directions: one mainly focused on high baseline torque, and one mainly focused on improved robustness under ASC operation.

5.2.1 Selection of Two Candidate Models

From the evaluated UI* configurations, the 8P-6H-48S model with 2PP and the 8P-8H-72S model with 3PP were selected as the two candidate models for preliminary optimization. The reason for selecting these two models was that they represented two different design behaviors, as shown in Figure 5.10.

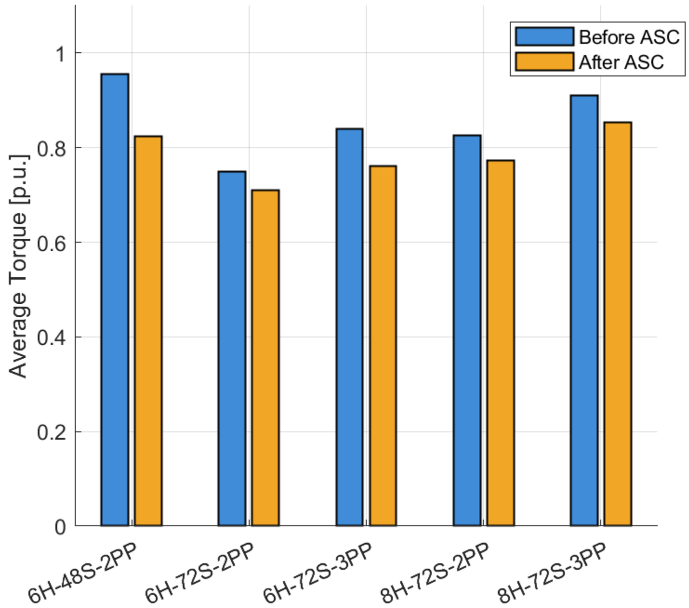

Figure 5.10: Selection of two candidate UI* configurations for preliminary optimization based on torque capability.

The 8P-6H-48S 2PP configuration was selected because it provided a strong baseline torque before ASC. However, its torque reduction was still relatively high, which made it a suitable candidate for investigating how much robustness could be improved through optimization.

The 8P-8H-72S 3PP configuration was selected because it showed a better balance between torque capability and demagnetization robustness. Compared with the other configurations, it provided relatively high torque while keeping the torque reduction close to 6%. This made it a strong candidate for developing a more fault-tolerant design.

In this way, the selected models represent two complementary optimization paths. The first model is more torque-oriented, while the second model is more robustness-oriented. The following section presents the preliminary optimization results for these two selected configurations.

5.2.2 Preliminary Optimization of the Selected Candidate Models

After selecting the two candidate models, a preliminary optimization was carried out to improve the ASC robustness without reducing the main torque performance. In this phase, the overall topology was kept unchanged, while selected geometrical parameters in the stator and rotor regions were modified. The changed parameters included conductor pin dimensions, slot-related dimensions, magnet position, magnet distance, and rotor flux path geometry. The purpose of changing these parameters was to improve the magnetic flux distribution around the magnets and reduce the local demagnetization concentration during ASC operation. Since the F45H magnet is more sensitive to irreversible demagnetization, small changes in magnet position and flux path geometry can strongly affect the final torque reduction after the fault condition. For the first selected candidate, the optimization was applied to the UI* 8P-6H-48S configuration with 2PP. Figure 5.11 compares the selected and optimized models under ASC operation at 130°C using F45H. The optimized design shows a more controlled demagnetization pattern, especially near the magnet edges.

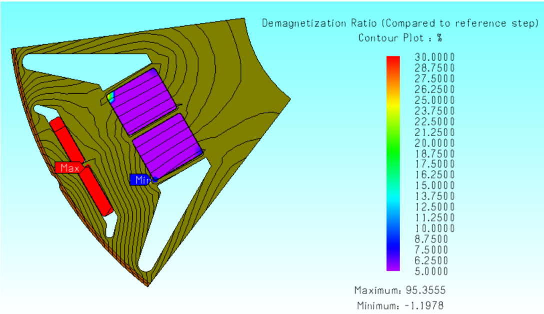

(a) Selected candidate

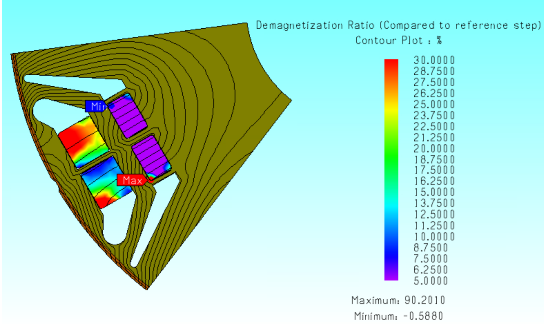

(b) Optimized model

Figure 5.11: Comparison between selected and optimized UI* 8P-6H-48S configuration under ASC operation at 130°C using F45H.

Table 5.6: Performance comparison of selected and optimized UI* 8P-6H-48S configuration under ASC operation at 130°C using F45H.

Model	**Torque before ASC (p.u.)**	**Torque after ASC (p.u.)**	**Torque Reduction (%)**
Selected candidate	0.956	0.824	13.73
Optimized model	1.001	0.953	4.78

Table 5.6 compares the torque performance before and after optimization for the first candidate. The torque reduction decreased from 13.73% to 4.78% after optimization. At the same time, the torque before ASC slightly increased from 0.956 p.u. to 1.001 p.u. This means that the robustness under ASC was improved without sacrificing the baseline torque capability. For the second selected candidate, the optimization was applied to the UI* 8P-8H-72S configuration with 3PP. The comparison between the selected and optimized geometries is shown in Figure 5.12. This model already had better ASC robustness before optimization, so the main target was to further reduce the torque drop while maintaining or improving the torque level.

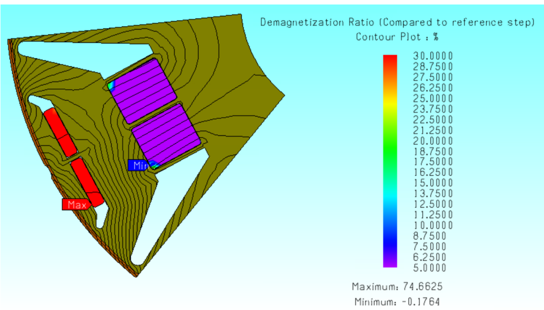

(a) Selected candidate

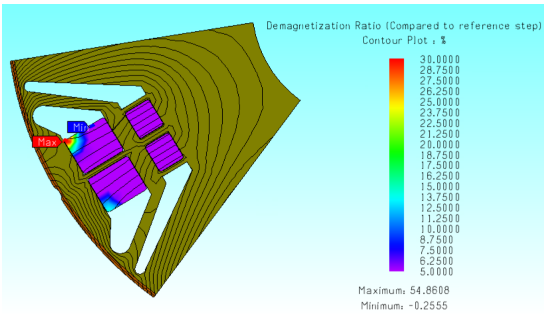

(b) Optimized model

Figure 5.12: Comparison between selected and optimized UI* 8P-8H-72S configuration under ASC operation at 130°C using F45H.

Table 5.7: Performance comparison of selected and optimized UI* 8P-8H-72S configuration under ASC operation at 130°C using F45H.

Model	**Torque before ASC (p.u.)**	**Torque after ASC (p.u.)**	**Torque Reduction (%)**
Selected candidate	0.911	0.855	6.15
Optimized model	0.939	0.931	0.8

The results in Table 5.7 show that the optimized model improved the ASC robustness of the second candidate. The torque reduction decreased from 6.15% to 0.8%, which indicates a clear improvement in demagnetization resistance after optimization. The torque before ASC also increased slightly from 0.911 p.u. to 0.939 p.u.; however, it remained lower than the optimized torque-oriented candidate. Therefore, the second candidate was mainly improved from a robustness point of view rather than from a maximum torque capability point of view.

Overall, the preliminary optimization confirmed that geometry modification can improve the behavior of F45H-based designs under ASC conditions. The first candidate showed improvement in both baseline torque capability and ASC robustness, while the second candidate lead to reduced amount of torque degradation after demag . These two optimized candidates therefore represent two different design directions: one more torque-oriented and the other more robustness-oriented.

5.2.3 Magnetic Flux Density and Torque-Speed Performance Analysis

Figure 5.13 compares the magnetic flux density distribution of the selected and optimized models for both candidate configurations. The results show that the optimization affects the flux distribution around the magnet edges, flux barriers, and airgap region. After optimization, the high flux density regions become more controlled, which can help reduce local saturation and improve the ASC robustness of the design.

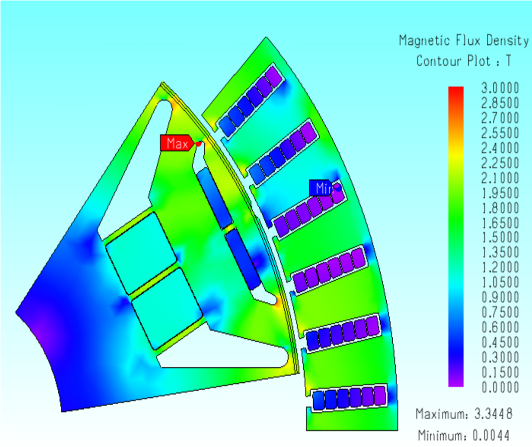

(a) Candidate configuration 1 – Selected

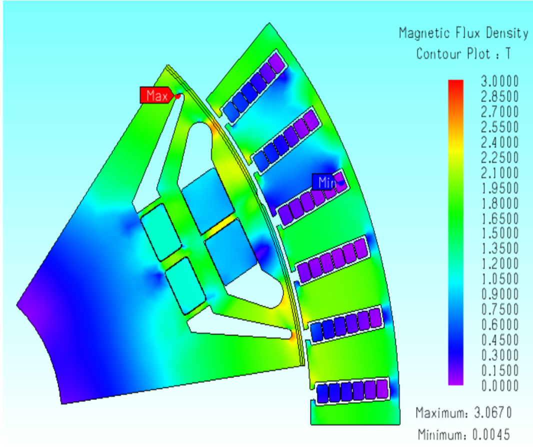

(b) Candidate configuration 1 – Optimized

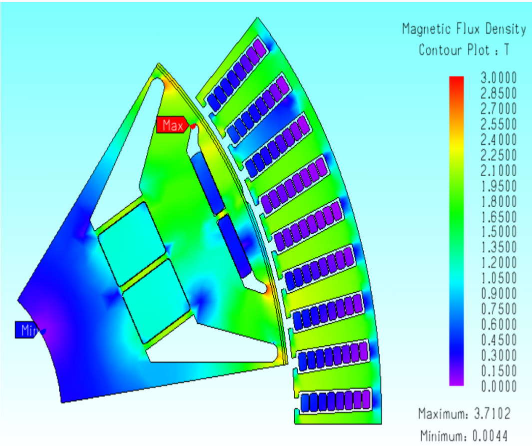

(c) Candidate configuration 2 – Selected

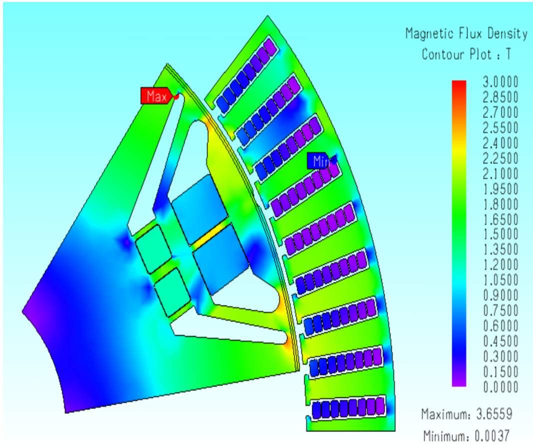

(d) Candidate configuration 2 – Optimized

Figure 5.13: Magnetic flux density comparison between selected and optimized models under ASC operation.

Figures 5.14 and 5.15 show the torque-speed and output power comparison of the two selected candidate configurations before and after preliminary optimization. The optimized version of candidate configuration 1 shows better torque retention and higher output power in the high-speed region, indicating improved flux-weakening capability. For candidate configuration 2, the main improvement appears around the transition region between constant-torque and field-weakening operation, while the high-speed difference is less significant. These results indicate that the preliminary optimization improved the overall operating performance of both selected candidates.

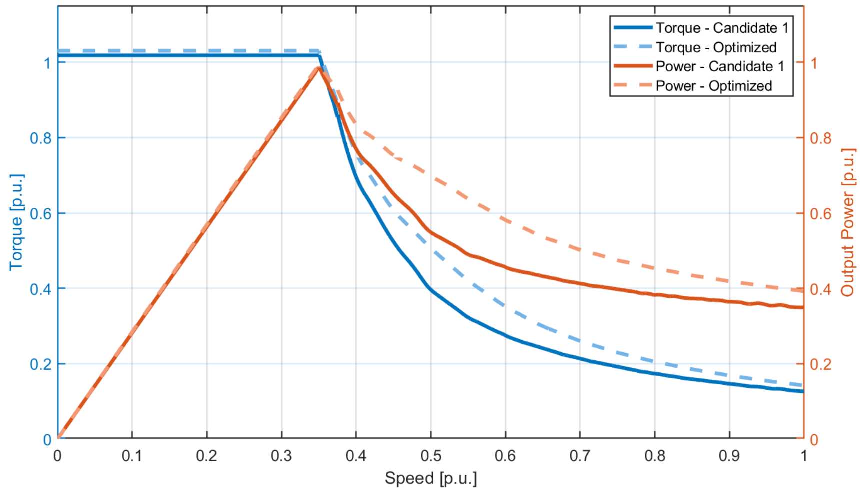

Figure 5.14: Torque-speed and output power comparison for candidate configuration 1.

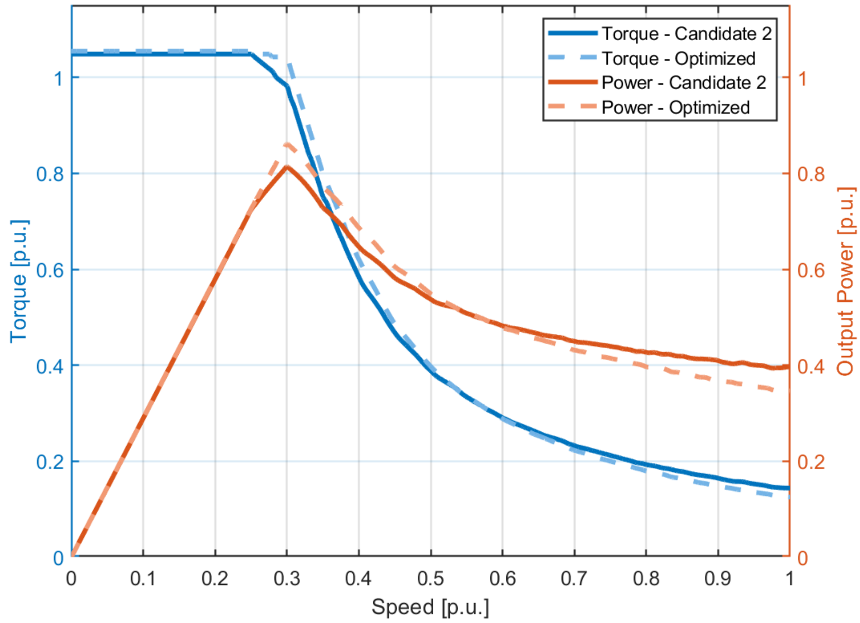

Figure 5.15: Torque-speed and output power comparison for candidate configuration 2.

The results of this chapter show that the UI* topology with HREE-free magnets is a feasible solution for improving ASC robustness while maintaining the main torque capability and high-speed performance. The preliminary optimization also confirmed that parameters such as slot configuration, hairpin arrangement, parallel path selection, and rotor geometry have a strong impact on both demagnetization behavior and electromagnetic performance.

Based on these results, the next chapter focuses on full-scale optimization of the selected candidate models in order to further improve efficiency, reduce magnet weight, and minimize irreversible demagnetization under severe operating conditions.

Chapter 6

Full-Scale Optimization and Final Candidate Evaluation

The previous chapter identified the most promising machine configurations through topology screening and preliminary parametric optimization. In this chapter, these candidate models are further improved using the multi objective genetic algorithm-based optimization and evaluated against the benchmark machine.

The objective of this stage is not only to improve the electromagnetic performance of the selected candidates, but also to investigate whether lower-cost magnet materials can achieve performance comparable to the benchmark machine while maintaining high robustness against ASC-induced demagnetization.

The optimization results are analyzed based on torque capability, efficiency, total losses, demagnetization behavior, material cost, and an equivalent WLTP-related loss based on selected operating points. The final objective is to identify the most suitable machine design based on the overall performance and cost trade-off.

6.1 Correlation and Trade-Off Analysis

The full-scale optimization studies generated several hundred candidate solutions for each investigated machine configuration.

The purpose of this analysis was to reduce the optimization database while preserving solutions that satisfied the required torque capability and showed acceptable efficiency, loss characteristics, and demagnetization robustness.

Correlation matrices were used to examine the relationships between the main design variables and the selected performance indicators. This analysis provided insight into the influence of individual parameters on torque capability, efficiency, losses, material usage, and demagnetization behaviour.

In addition, trade-off plots were used to identify candidate designs that achieved a balanced compromise between electromagnetic performance and cost-related objectives. The evaluation considered the combined influence of torque capability, losses, efficiency, demagnetization robustness, and material utilization.

Based on the combined correlation and trade-off analyses, five representative candidates were selected from each optimization study and carried forward for detailed electromagnetic evaluation. The selected candidates are evaluated in the following sections.

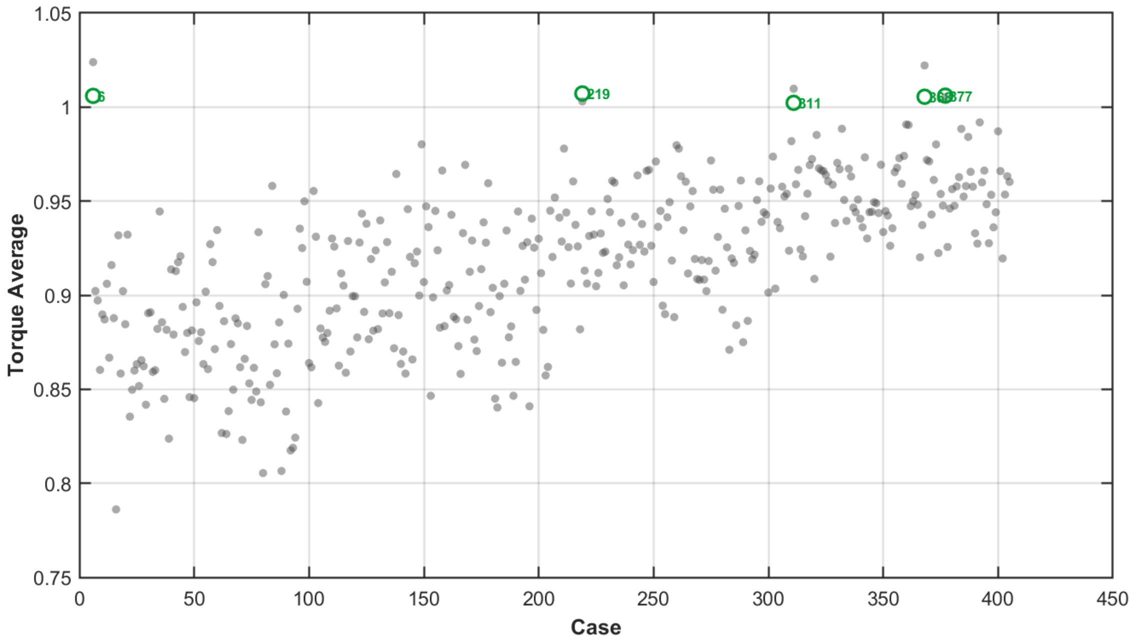

Figure 6.1: Representative candidates selected from the optimization database for detailed evaluation.

6.1.1 Correlation Matrix Analysis

The full-scale optimization generated several hundred design candidates for the investigated machine configuration. To reduce the solution space and identify promising candidates, a correlation-based analysis was first performed between the main geometric design variables and the selected performance indicators.

The objective of this step was not to select the final design directly, but rather to understand how individual parameters influence torque capability, efficiency, losses, material utilization, and demagnetization-related behaviour. This information was subsequently used to guide the candidate screening process.

Figure 6.2 presents an example of the correlation matrix obtained for the 8P-8H-72S-F45H optimization study. The matrix highlights the relative influence of the investigated design variables on the main electromagnetic performance indicators and provides useful insight into the dominant design trends observed within the optimization database.

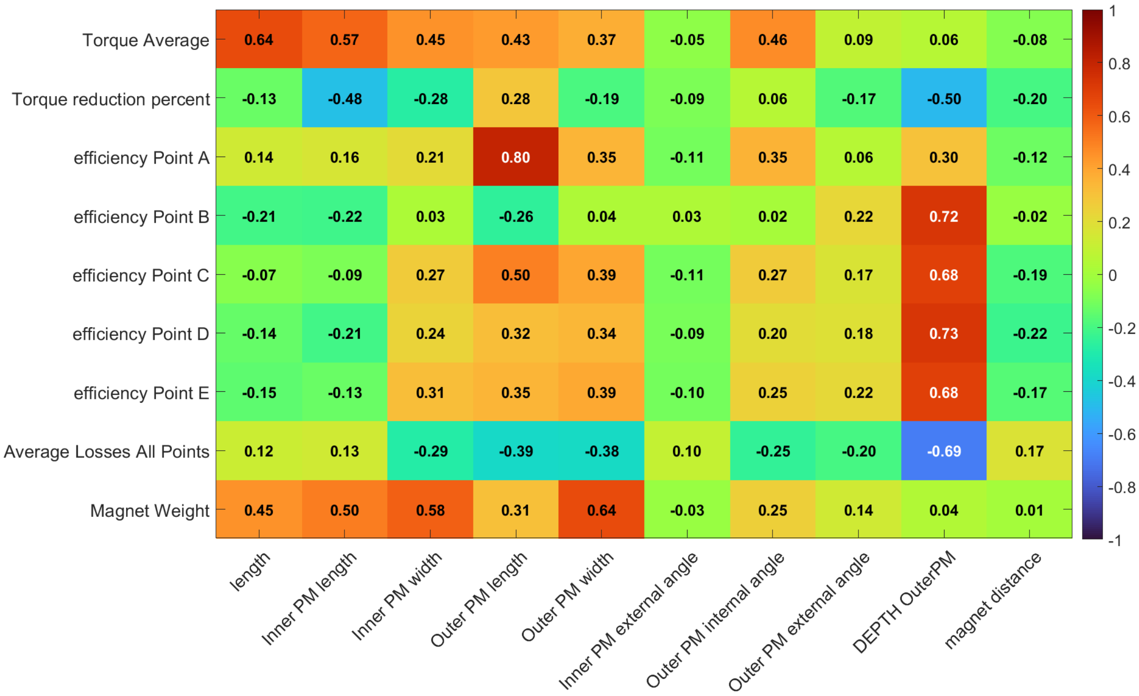

Figure 6.2: Correlation matrix obtained from the optimization database of the 8P-8H-72S-F45H configuration.

The correlation analysis served as a qualitative tool for interpreting the optimization results and for identifying parameter combinations that were more likely to satisfy the required performance targets.

6.1.2 Trade-Off Analysis

After the correlation study, a trade-off analysis was carried out to identify candidate solutions that simultaneously satisfied the electromagnetic and cost-oriented objectives.

Instead of selecting candidates solely based on maximum torque or minimum cost, the evaluation considered the overall balance between torque capability, efficiency, losses, material utilization, and robustness-related indicators. This approach helped avoid solutions that performed well in a single objective while exhibiting weaker behaviour in other important criteria.

Figure 6.3 shows an example of the trade-off evaluation performed for the 8P-8H-72S-F45H optimization study. Each point represents one optimization candidate, while the highlighted points correspond to the representative candidates selected for detailed evaluation in the following sections.

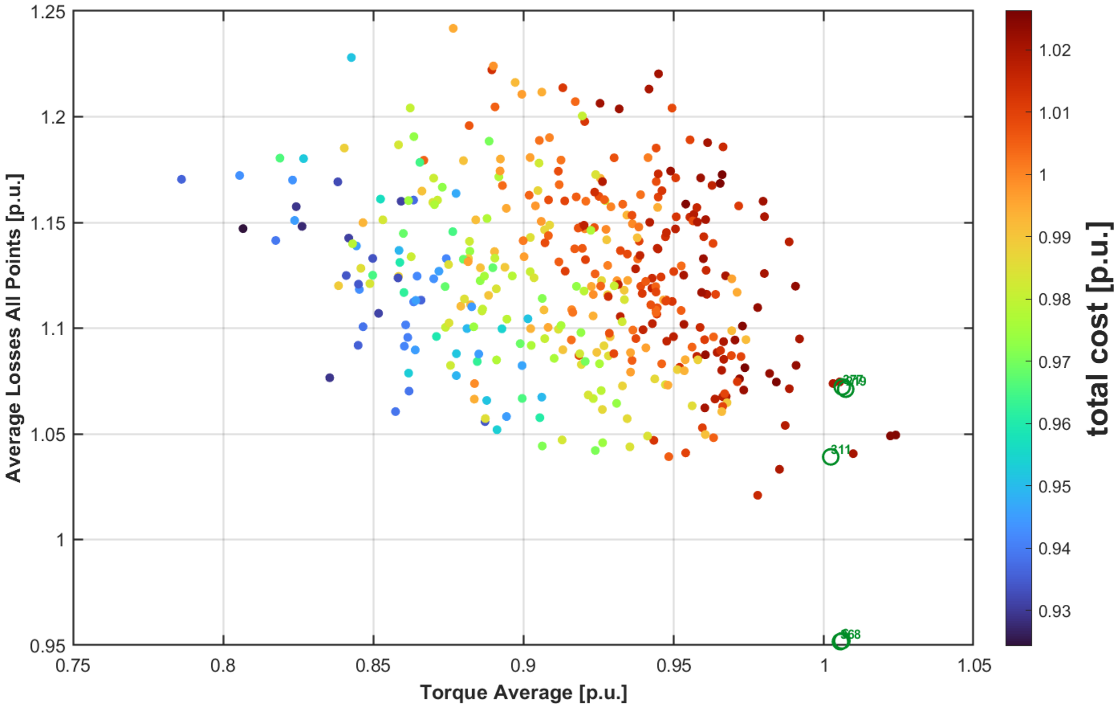

Figure 6.3: Example of the trade-off analysis used for candidate screening in the 8P-8H-72S-F45H optimization study.

Based on this analysis, five representative candidates were selected from the optimization database and carried forward for detailed electromagnetic comparison.

The same methodology was applied to all investigated machine configurations. The selected candidates were subsequently evaluated through detailed electromagnetic analyses, and one final design was chosen based on the overall balance between performance, efficiency, robustness, and cost.

6.2 Optimization Results of the 8P-6H-48S Configuration

The optimized 8P-6H-48S configuration obtained from the preliminary optimization stage was selected as the first candidate for full-scale optimization. The objective of this stage was to investigate whether the selected topology could achieve the required torque level while maintaining low demagnetization, efficiency, and competitive cost performance when compared with the benchmark machine.

The optimization process was carried out separately for the F45H and F48SH magnet materials. For each magnet type, several hundred design candidates were generated during the optimization. The generated solutions were evaluated using the objective functions described in Chapter 4 and ranked according to torque capability, demagnetization robustness, efficiency, and cost-related criteria.

From the generated solutions, five representative candidates were selected for detailed investigation. These candidates were chosen based on their overall trade-off between electromagnetic performance and cost-oriented design objectives.

6.2.1 Evaluation of F45H Magnet Solutions

The full-scale optimization of the 8P-6H-48S model was first performed using the F45H magnet. Five representative cases were selected from the optimization results and compared with the benchmark model. The selected design parameters are summarized in Table 6.1, while the main performance indicators are given in Table 6.2.

Table 6.1: Design and material summary of the 8P-6H-48S configuration using F45H magnet.

Model	**Stack Length (p.u.)**	**Total Weight (p.u.)**	**Magnet Weight (p.u.)**	**Material Cost (p.u.)**
Case BM	1.00	1.00	1.00	1.00
Case 6	1.10	1.10	1.06	1.04
Case 153	1.10	1.10	1.06	1.05
Case 323	1.10	1.10	1.06	1.05
Case 370	1.10	1.10	1.06	1.05
Case 397	1.10	1.10	1.06	1.05

Table 6.2: Final KPI summary of the 8P-6H-48S configuration using F45H magnet.

Model	**Avg Torque (p.u.)**	**Torque Reduction (%)**	**Avg Loss (p.u.)**	**Equivalent WLTP Loss (p.u.)**	**Total Cost (p.u.)**
Case BM	1.01	0.00	1.00	1.00	1.00
Case 6	1.00	0.78	1.02	1.02	1.07
Case 153	1.00	0.92	1.02	1.02	1.07
Case 323	1.00	0.92	1.02	1.02	1.07
Case 370	1.00	0.92	1.02	1.02	1.08
Case 397	1.00	0.92	1.02	1.02	1.07

Figure 6.4 shows the total costs of the selected cases compared with the benchmark reference. All selected cases remain above the benchmark level, which indicates that the optimized F45H solutions do not provide a cost advantage for this configuration. The torque results show that the average torque is maintained close to 1 p.u., while the torque reduction after ASC remains below 1%. Therefore, the electromagnetic robustness is improved, but this improvement is not enough to compensate for the higher cost-oriented index.

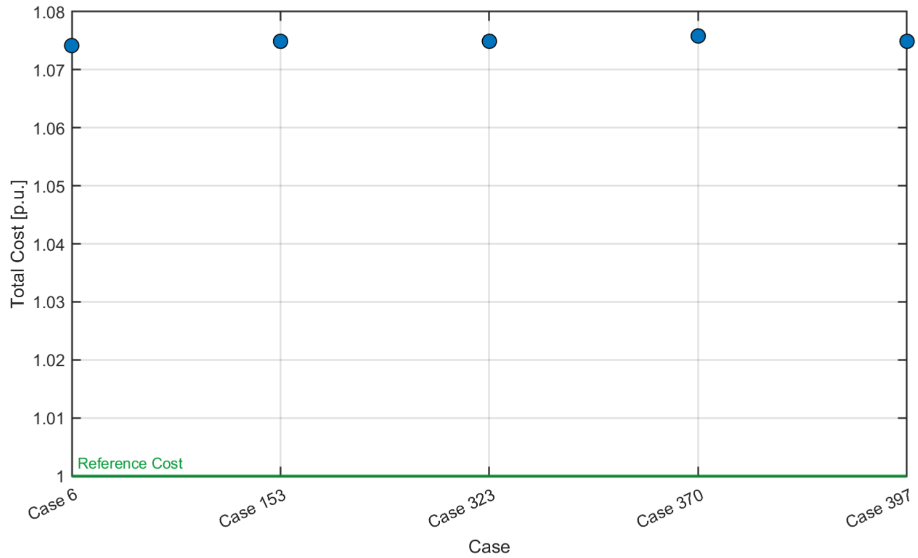

Figure 6.4: Total cost comparison for the 8P-6H-48S configuration using F45H magnet.

The efficiency comparison in Figure 6.5 shows that the selected cases remain close to the benchmark at most operating points. However, Figure 6.6 shows that these cases have slightly higher operating-point losses and a higher equivalent WLTP loss indicator compared with the benchmark. This increases the loss-related contribution to the total cost. Therefore, based on the overall cost-oriented evaluation, the 8P-6H-48S configuration using the F45H magnet was not selected for the final candidate stage.

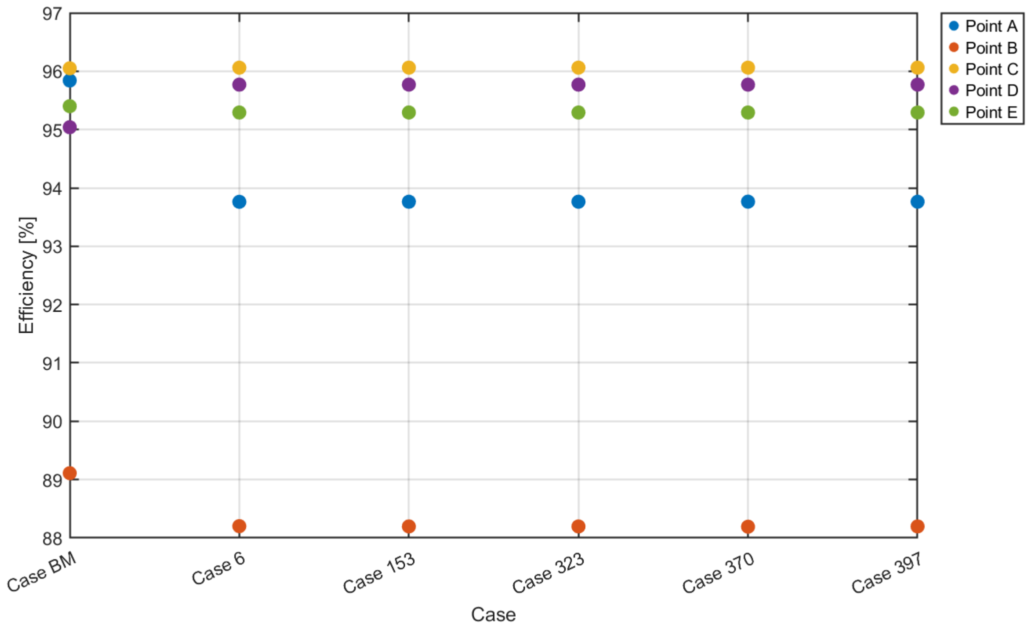

Figure 6.5: Efficiency comparison at the selected operating points for the 8P-6H-48S configuration using F45H magnet.

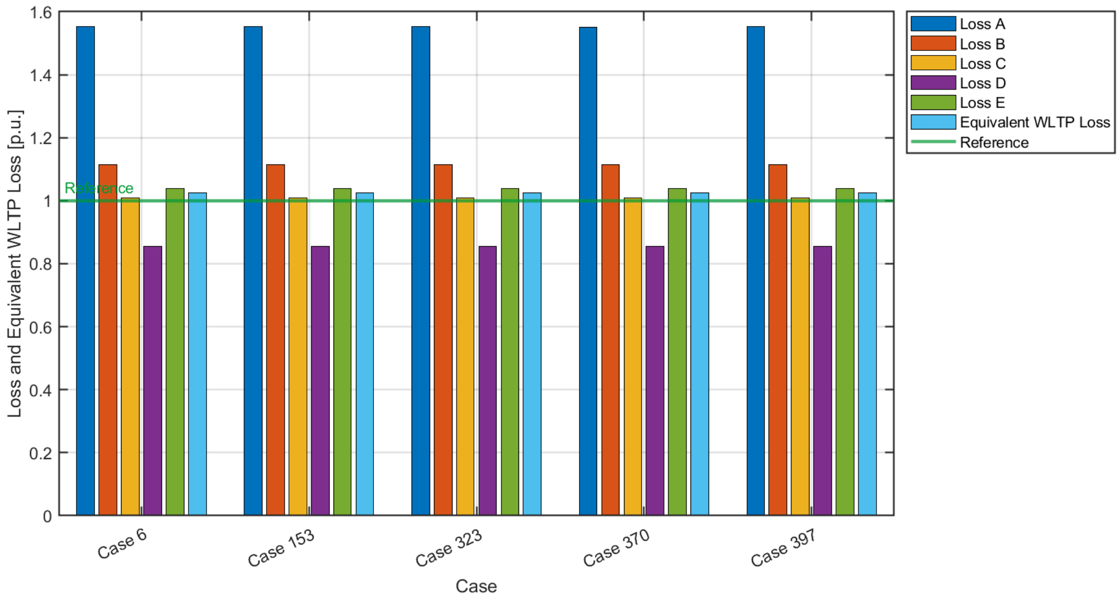

Figure 6.6: Operating-point loss and equivalent WLTP loss indicator comparison for the 8P-6H-48S configuration using the F45H magnet.

6.2.2 Evaluation of F48SH Magnet Solutions

The same optimization procedure was repeated for the 8P-6H-48S configuration using the F48SH magnet. The selected cases are summarized in Table 6.3 and Table 6.4.

Table 6.3: Design and material summary of the 8P-6H-48S configuration using F48SH magnet.

Model	Stack Length (p.u.)	Total Weight (p.u.)	Magnet Weight (p.u.)	Material Cost (p.u.)
Case BM	1.00	1.00	1.00	1.00
Case 12	1.07	1.06	1.12	1.04
Case 159	1.08	1.08	0.98	1.04
Case 327	1.07	1.06	1.13	1.04
Case 213	1.08	1.08	1.04	1.04
Case 361	1.08	1.07	1.12	1.05

Table 6.4: Final KPI summary of the 8P-6H-48S configuration using F48SH magnet.

Model	Avg Torque (p.u.)	Torque Reduction (%)	Avg Loss (p.u.)	Equivalent WLTP Loss (p.u.)	Total Cost (p.u.)
Case BM	1.01	0.00	1.00	1.00	1.00
Case 12	1.01	0.09	1.05	1.05	1.10
Case 159	1.00	0.06	1.02	1.02	1.06
Case 327	1.00	0.18	1.02	1.02	1.07
Case 213	1.00	0.01	1.05	1.05	1.10
Case 361	1.00	0.13	1.00	1.00	1.06

Compared with the F45H results, the F48SH magnet is expected to provide better demagnetization robustness because of its stronger magnetic resistance under ASC conditions. The selected optimized cases are compared in term of total costs in Figure 6.7 .

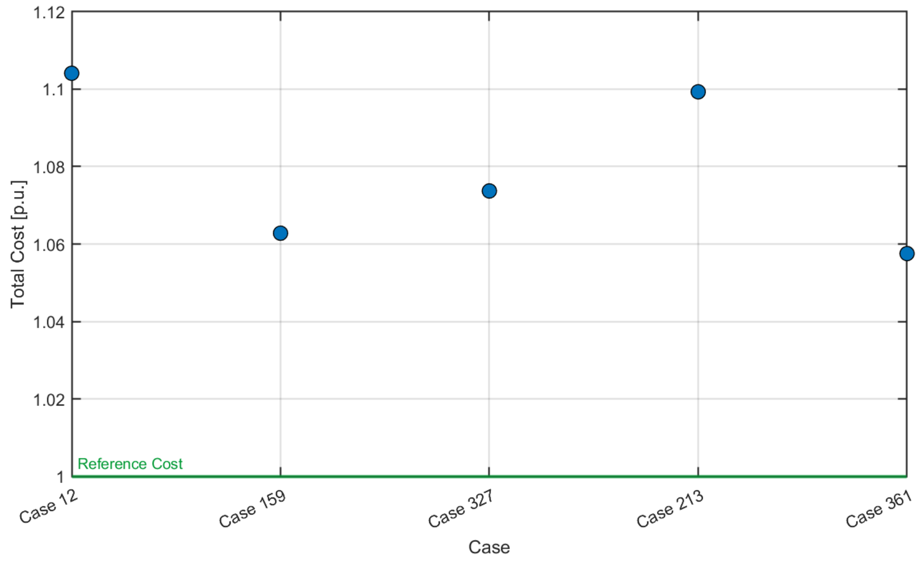

Figure 6.7: total costs comparison for the 8P-6H-48S configuration using F48SH magnet.

The efficiency and loss-based results are shown in Figure 6.8 and Figure 6.9. Although the F48SH solutions improve ASC robustness, the total costs is still evaluated against the benchmark reference. If the total costs remains above 1 p.u., the configuration is not carried forward as the final selected candidate.

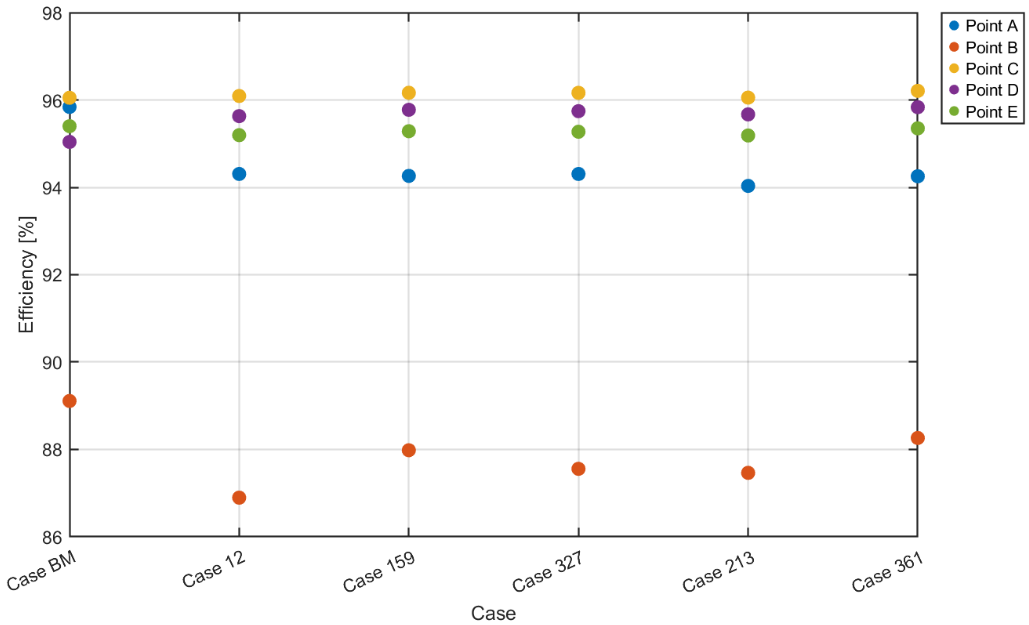

Figure 6.8: Efficiency comparison at the selected operating points for the 8P-6H-48S configuration using F48SH magnet.

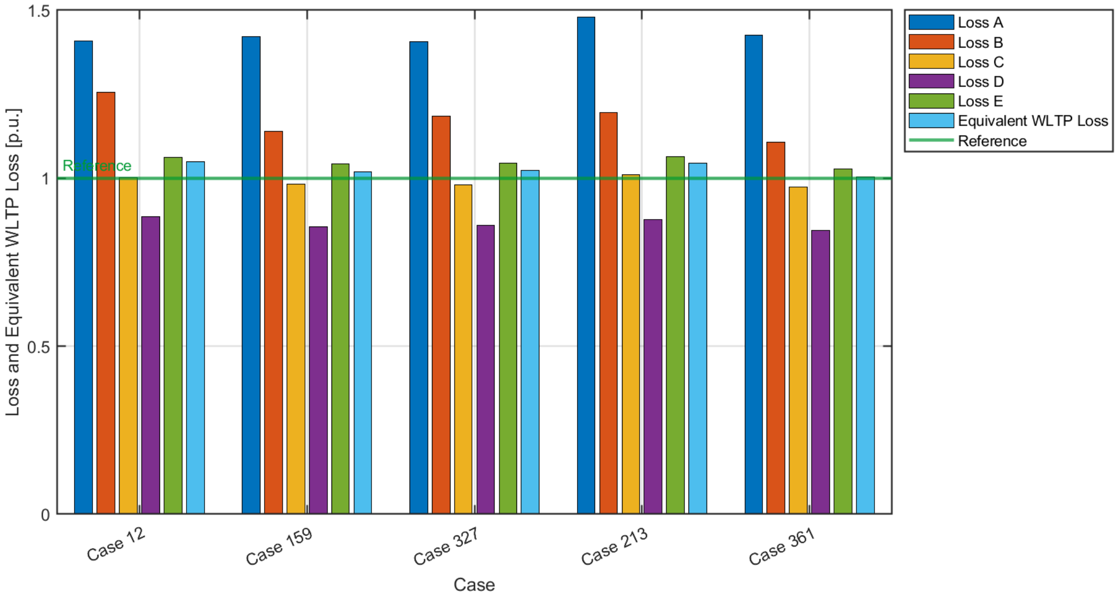

Figure 6.9: Operating-point loss and equivalent WLTP loss indicator comparison for the 8P-6H-48S configuration using the F48SH magnet.

Overall, the 8P-6H-48S configuration shows acceptable electromagnetic performance after optimization. However, the cost-oriented evaluation indicates that this configuration does not provide a better overall trade-off than the benchmark model. Therefore, the next evaluation step focuses on the 8P-8H-72S configuration.

6.3 Optimization Results of the 8P-8H-72S Configuration

After evaluating the 8P-6H-48S configuration, the same full-scale optimization procedure was applied to the second selected candidate, the 8P-8H-72S configuration. This model was included because the higher number of hairpin layers and stator slots provides additional design flexibility and can improve the electromagnetic loading of the machine.

The optimization was performed separately using F45H and F48SH magnets. Similar to the previous configuration, five representative cases were selected for each magnet type based on torque capability, ASC robustness, loss behavior, equivalent drive cycle efficiency-related performance, and the total cost/business value . The results are presented in the following subsections.

6.3.1 Evaluation of F45H Magnet Solutions

The full-scale optimization of the 8P-8H-72S configuration was first performed using the F45H magnet. The selected design parameters and the final KPI summary are presented in Table 6.5 and Table 6.6, respectively.

Table 6.5: Design and material summary of the 8P-8H-72S configuration using F45H magnet.

Model	Stack Length (p.u.)	Total Weight (p.u.)	Magnet Weight (p.u.)	Material Cost (p.u.)
Case BM	1.00	1.00	1.00	1.00
Case 6	1.03	1.01	1.08	1.02
Case 219	1.03	1.02	1.03	1.02
Case 311	1.02	1.01	1.06	1.01
Case 368	1.03	1.01	1.08	1.02
Case 377	1.03	1.02	1.03	1.02

Table 6.6: Final KPI summary of the 8P-8H-72S configuration using F45H magnet.

Model	Avg Torque (p.u.)	Torque Reduction (%)	Avg Loss (p.u.)	Equivalent WLTP Loss (p.u.)	Total Cost (p.u.)
Case BM	1.01	0.00	1.00	1.00	1.00
Case 6	1.01	0.93	0.95	0.95	0.96
Case 219	1.01	1.05	1.07	1.07	1.10
Case 311	1.00	0.83	1.04	1.04	1.06
Case 368	1.01	0.92	0.95	0.95	0.96
Case 377	1.01	1.06	1.07	1.07	1.11

Figure 6.10 compares the total costs of the selected F45H cases with the benchmark reference. The optimized cases maintain the required torque level, while the torque reduction after ASC remains low, indicating that the geometry optimization improves the robustness of the design.

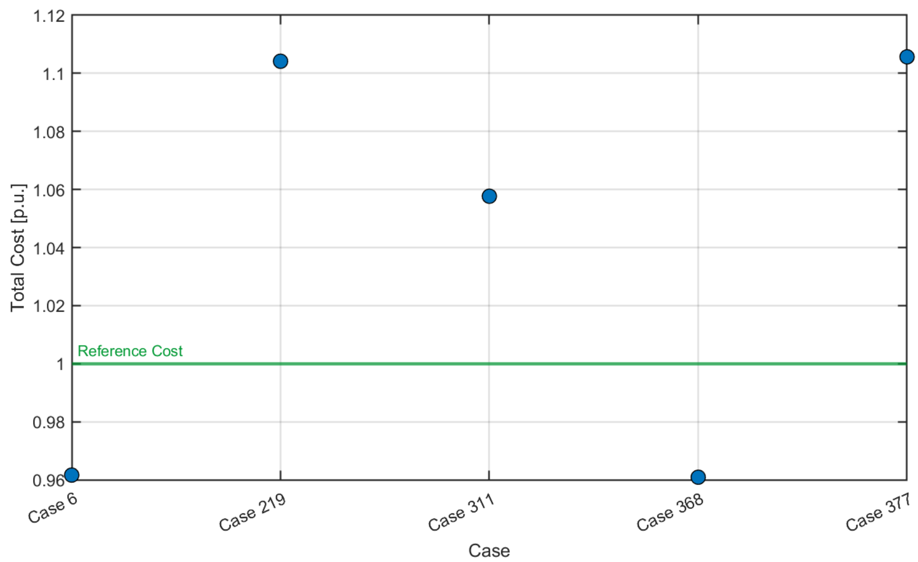

Figure 6.10: Total costs comparison for the 8P-8H-72S configuration using F45H magnet.

The efficiency and loss-related results are shown in Figure 6.11 and Figure 6.12. Compared with the previous 8P-6H-48S configuration, this model provides a more promising balance between electromagnetic performance and the cost-oriented evaluation. Some cases show a lower total costs than the benchmark reference, which makes this configuration relevant for the final selection stage.

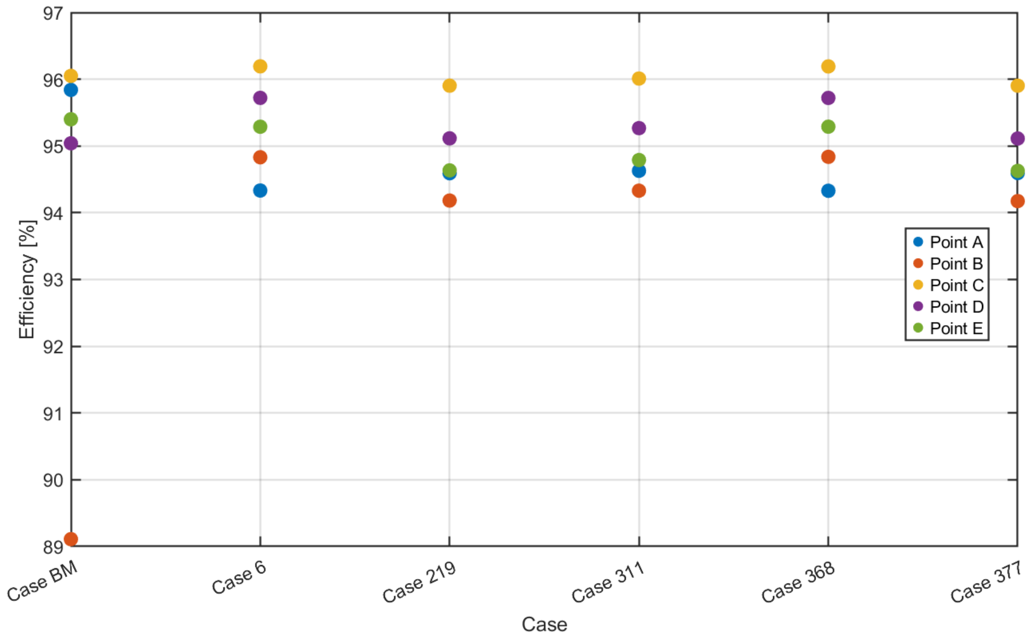

Figure 6.11: Efficiency comparison at the selected operating points for the 8P-8H-72S configuration using F45H magnet.

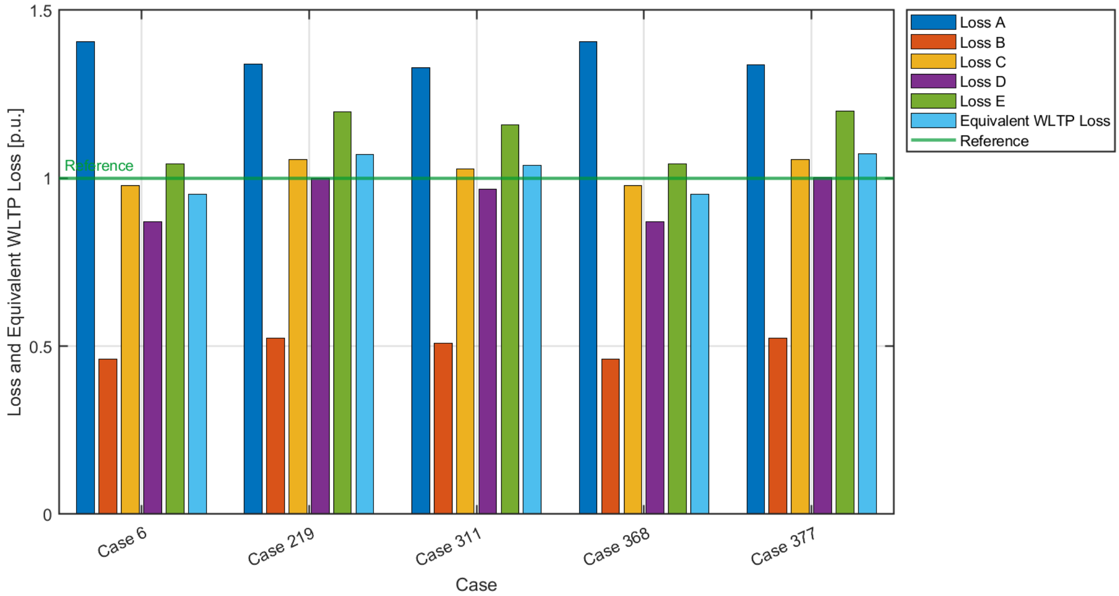

Figure 6.12: Operating-point loss and equivalent WLTP loss indicator comparison for the 8P-8H-72S configuration using the F45H magnet.

6.3.2 Evaluation of F48SH Magnet Solutions

The same optimization procedure was repeated for the 8P-8H-72S configuration using the F48SH magnet. The selected design parameters and final KPIs are summarized in Table 6.7 and Table 6.8.

Table 6.7: Design and material summary of the 8P-8H-72S configuration using F48SH magnet.

Model	Stack Length (p.u.)	Total Weight (p.u.)	Magnet Weight (p.u.)	Material Cost (p.u.)
Case BM	1.00	1.00	1.00	1.00
Case 6	1.01	1.00	1.06	1.02
Case 130	1.01	1.00	1.04	1.02
Case 206	1.02	1.00	1.07	1.03
Case 337	1.03	1.02	1.02	1.03
Case 339	1.02	1.01	1.06	1.03

Table 6.8: Final KPI summary of the 8P-8H-72S configuration using F48SH magnet.

Model	Avg Torque (p.u.)	Torque Reduction (%)	Avg Loss (p.u.)	Equivalent WLTP Loss (p.u.)	Total Cost (p.u.)
Case BM	1.01	0.00	1.00	1.00	1.00
Case 6	1.00	0.09	0.95	0.95	0.96
Case 130	1.00	0.07	1.02	1.02	1.05
Case 206	1.00	0.02	0.95	0.95	0.97
Case 337	1.00	0.12	1.02	1.02	1.05
Case 339	1.00	0.04	0.99	0.99	1.02

Figure 6.13 shows the total costs of the selected F48SH cases. The F48SH magnet generally provides stronger demagnetization resistance, while the final decision also depends on loss behavior and cost-oriented performance.

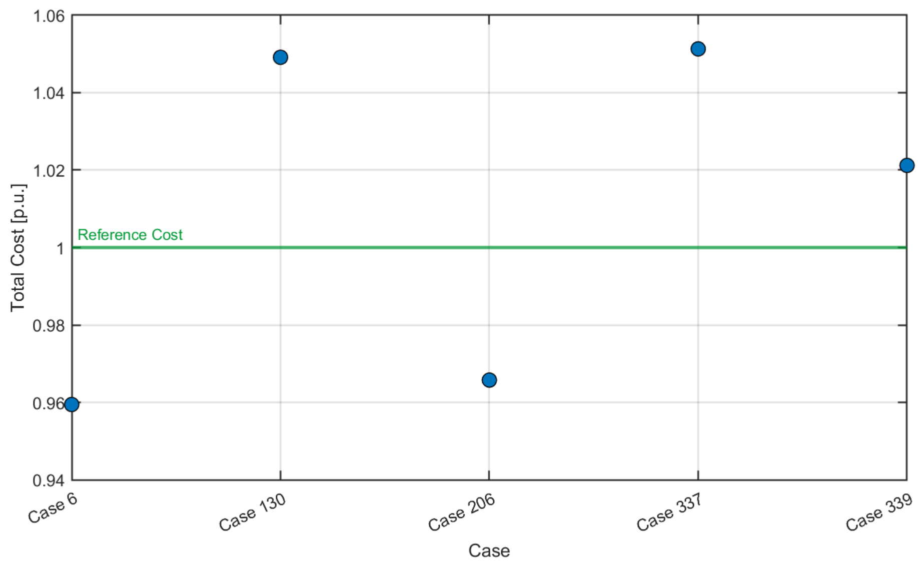

Figure 6.13: Total costs comparison for the 8P-8H-72S configuration using F48SH magnet.

The efficiency comparison and the equivalent WLTP loss evaluation for the 8P-8H-72S configuration using the F48SH magnet are shown in Figures 6.14 and 6.15, respectively. These results are considered together with the F45H results in the final candidate selection presented in the following section.

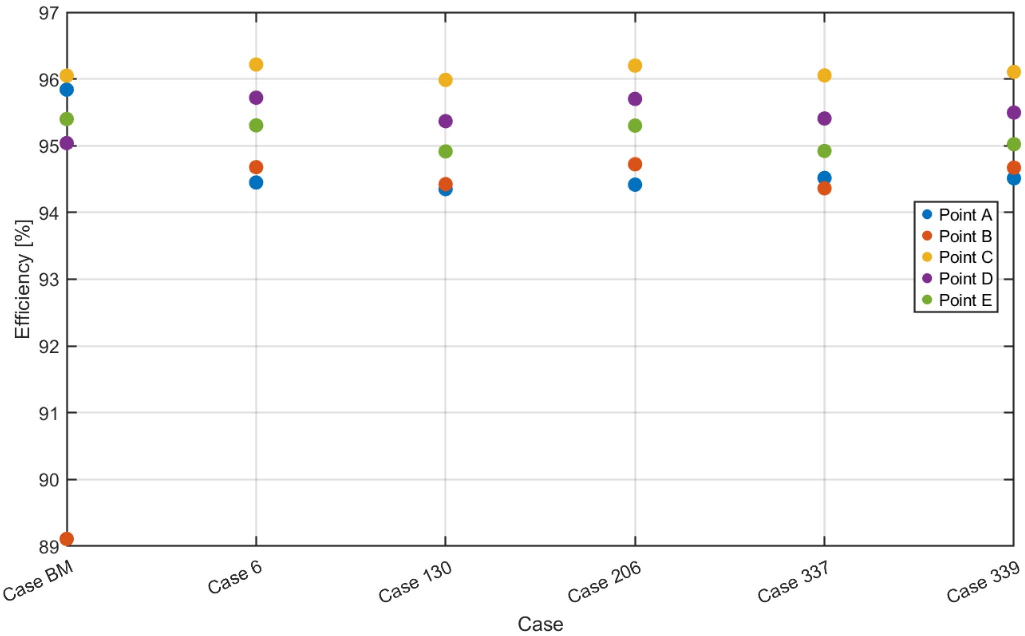

Figure 6.14: Efficiency comparison at the selected operating points for the 8P-8H-72S configuration using F48SH magnet.

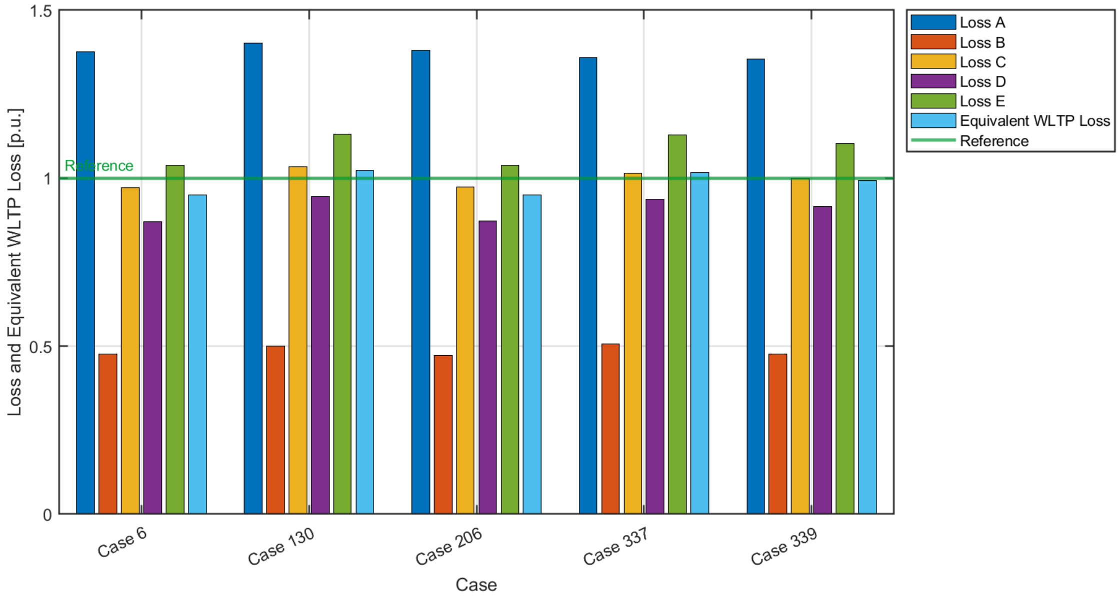

Figure 6.15: Operating-point loss and equivalent WLTP loss indicator comparison for the 8P-8H-72S configuration using the F48SH magnet.

6.4 Optimized Benchmark-Based VV Configuration with F45H Magnet

In addition to the UI* candidate configurations, the benchmark-based VV rotor model was also optimized using the F45H magnet. This study was performed to evaluate whether the original benchmark-type topology could benefit from the lower-cost F45H magnet material when the same optimization framework was applied.

The Genetic Algorithm optimization module was used to generate a new set of design cases, and five representative candidates were selected for detailed comparison. The selected design parameters are summarized in Table 6.9, while the corresponding final KPIs are shown in Table 6.10.

Table 6.9: Design and material summary of the optimized benchmark-based VV configuration using F45H magnet.

Model	**Stack Length (p.u.)**	**Total Weight (p.u.)**	**Magnet Weight (p.u.)**	**Material Cost (p.u.)**
Case BM	1.00	1.00	1.00	1.00
Case 5	1.00	1.00	0.94	0.95
Case 23	1.01	1.01	0.93	0.96
Case 151	0.99	0.99	0.98	0.95
Case 215	1.00	1.00	0.92	0.95
Case 288	1.00	1.00	0.98	0.95

Table 6.10: Final KPI summary of the optimized benchmark-based VV configuration using F45H magnet.

Model	**Avg Torque (p.u.)**	**Avg Loss (%)**	**Equivalent WLTP Loss (p.u.)**	**Total Cost (p.u.)**
Case BM	1.01	1.00	1.00	1.00
Case 5	1.02	0.99	0.99	0.94
Case 23	1.01	0.99	0.99	0.94
Case 151	1.02	1.00	1.00	0.95
Case 215	1.02	0.99	0.99	0.94
Case 288	1.02	0.99	0.99	0.94

Figure 6.16 shows the total costs of the optimized benchmark-based VV cases. Since the F45H magnet has a lower material cost than the original benchmark magnet, several optimized cases show improved cost-oriented performance compared with the benchmark reference. However, the final comparison must also consider torque capability, average losses, equivalent WLTP-based loss behavior, and ASC robustness.

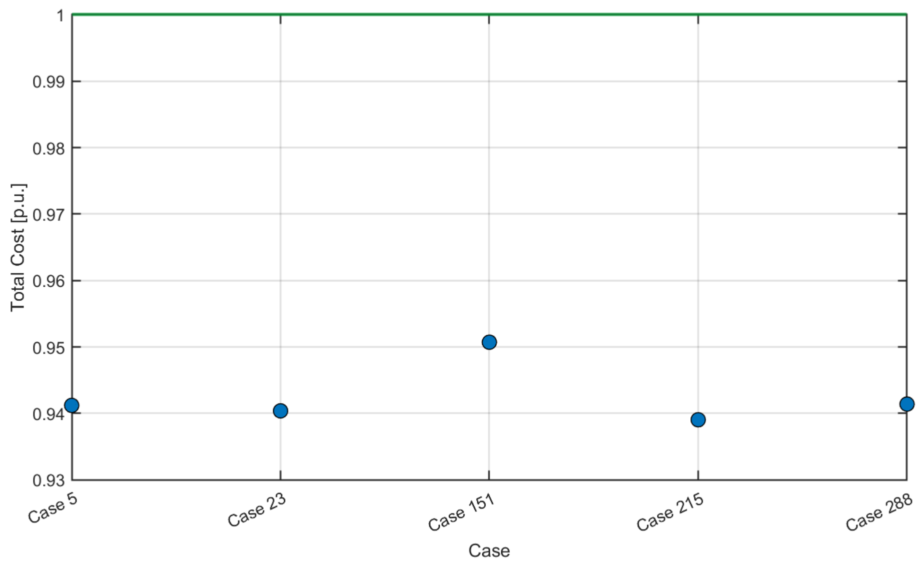

Figure 6.16: Total costs comparison for the optimized benchmark-based VV configuration using F45H magnet.

The efficiency comparison and equivalent WLTP loss evaluation are presented in Figure 6.17 and Figure 6.18. These results provide an additional reference for the final selection because they show how much improvement can be achieved by applying the same optimization strategy to a benchmark-based topology.

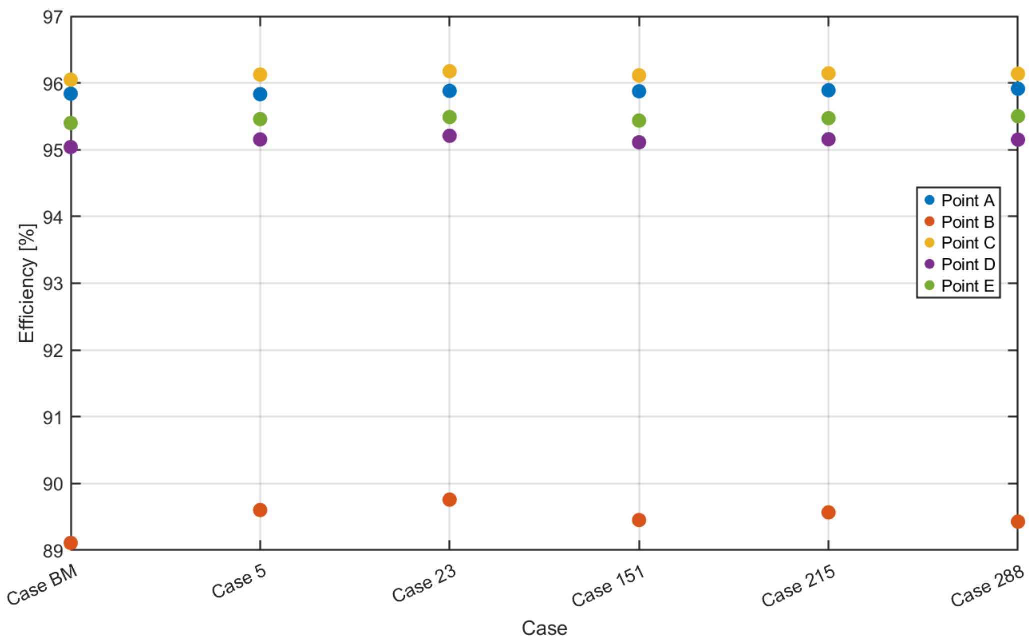

Figure 6.17: Efficiency comparison at the selected operating points for the optimized benchmark-based VV configuration using F45H magnet.

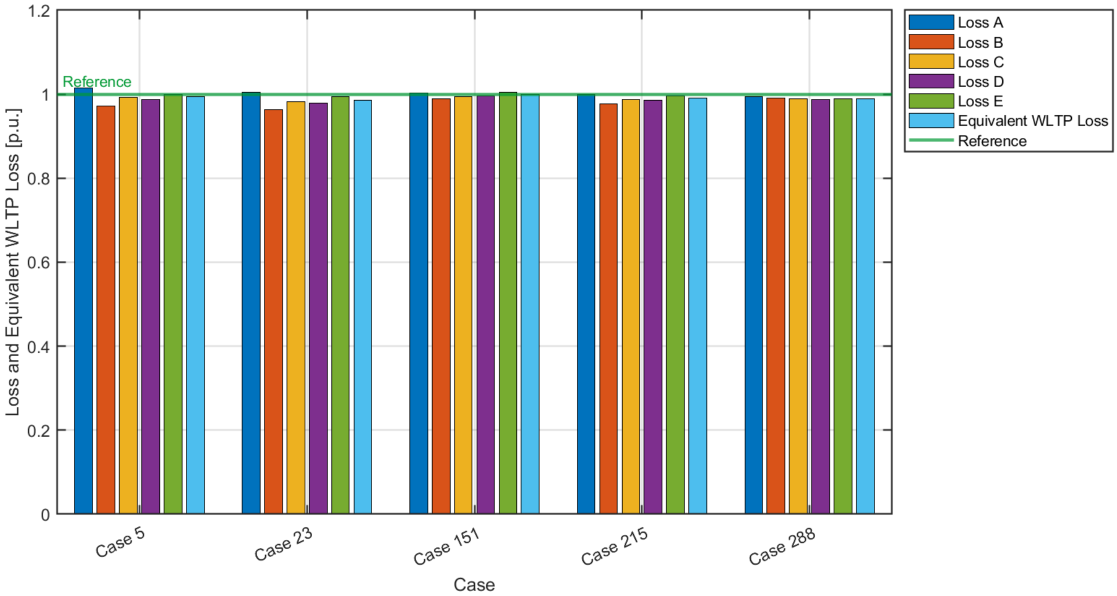

Figure 6.18: Operating-point loss and equivalent WLTP loss indicator comparison for the optimized benchmark-based VV configuration using F45H magnet.

The optimized benchmark-based VV configuration provides a useful comparison case for evaluating whether the newly proposed UI* candidates offer a better overall trade-off than improving the original topology with a lower-cost magnet material. The final selection between these alternatives is discussed in the next section.

6.5 Final Candidate Selection

After the detailed evaluation of each optimized model group, one representative candidate was selected from each group for the final comparison. The selection was mainly based on the total costs , followed by efficiency at the selected operating points, total losses, torque capability, demagnetization behaviour, and stack length.

The best representative candidates from the investigated groups are summarized in Table 6.11. The 8P-6H-48S candidates were not selected for the final design stage because their total costs remained higher than the benchmark reference. They are still included in the shortlist to show the complete filtering process.

The optimized benchmark-based VV model with F45H magnet showed the lowest total costs among all investigated cases. However, this model was mainly used as a benchmark-derived reference to evaluate the effect of replacing the original magnet material within the existing topology. Since the main objective of this thesis is to identify an improved machine configuration beyond the benchmark topology, the VV-based solution was not selected as the final candidate.

Among the redesigned UI* candidates, the 8P-8H-72S configuration using F45H magnet, Case 368, provided the best overall balance. It achieved a lower total costs than the benchmark, reduced average losses and Equivalent WLTP losses, maintained the required torque level, and showed acceptable ASC robustness. Therefore, Case 368 was selected as the final candidate for the benchmark comparison.

Table 6.11: Shortlist of the best representative candidates from each optimized model group.

Model Group	**Selected Case**	**Avg Torque (p.u.)**	**Torque Red. (%)**	**Avg Loss (p.u.)**	**Equivalent WLTP Loss (p.u.)**	**Total Cost (p.u.)**
8P-6H-48S-F45H	Case 6	1.00	0.78	1.02	1.02	1.07
8P-6H-48S-F48	Case 361	1.00	0.13	1.00	1.00	1.06
8P-8H-72S-F45H	Case 368	1.01	0.92	0.95	0.95	0.96
8P-8H-72S-F48	Case 6	1.00	0.09	0.95	0.95	0.96
VV-BM-F45H	Case 215	1.02	–	0.99	0.99	0.94

Table 6.11 shows that both 8P-8H-72S candidates provide a clear improvement compared with the 8P-6H-48S alternatives. Although the VV-BM-F45H case gives a lower total costs, it does not represent a new topology solution and was therefore treated as a reference case rather than a final redesigned candidate.

Based on this selection logic, the 8P-8H-72S-F45H Case 368 was chosen as the final optimized machine design. The next section compares this selected candidate directly with the benchmark machine.

6.6 Benchmark Comparison

After the final candidate selection process, Case 368 was identified as the optimum design among all investigated candidates. The selected 8P-8H-72S-F45H configuration provided the best overall balance between torque capability, efficiency performance, ASC robustness, and total cost.

The benchmark machine is used as the reference for all normalized comparisons presented in this section. The objective is to verify that the selected candidate maintains the required electromagnetic performance while improving the overall cost-performance balance.

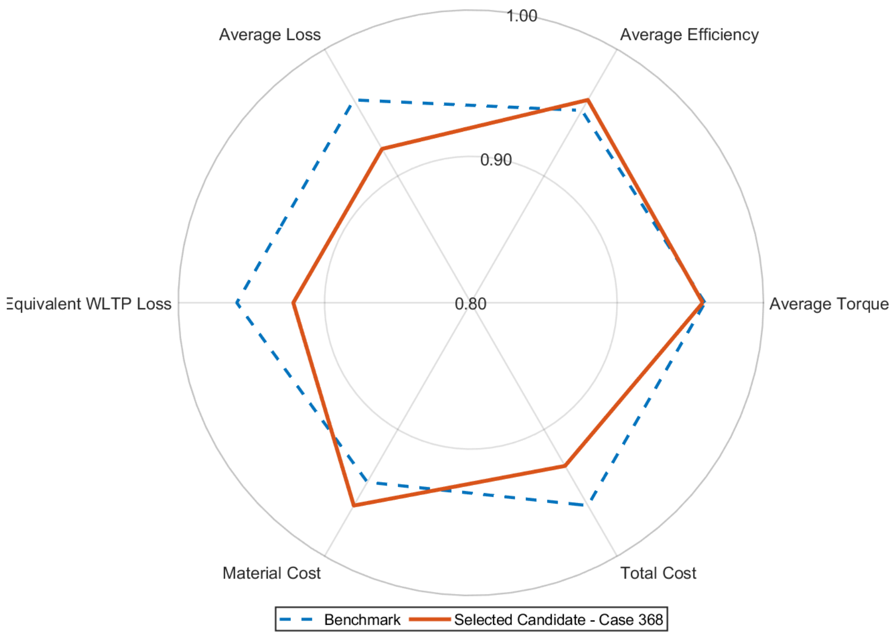

Figure 6.19: Radar chart comparison between the benchmark machine and the selected 8P-8H-72S-F45H Case 368.

Figure 6.19 provides an overall comparison between the benchmark machine and the selected candidate. The selected design maintains a torque capability and efficiency level close to the benchmark while improving the equivalent WLTP loss and total cost. This confirms that the optimization process achieved a better overall performance balance without compromising the key electromagnetic requirements.

6.6.1 Efficiency Comparison

The efficiency performance was evaluated using both the selected operating points defined in Chapter 4 and the wider efficiency map of the machine.

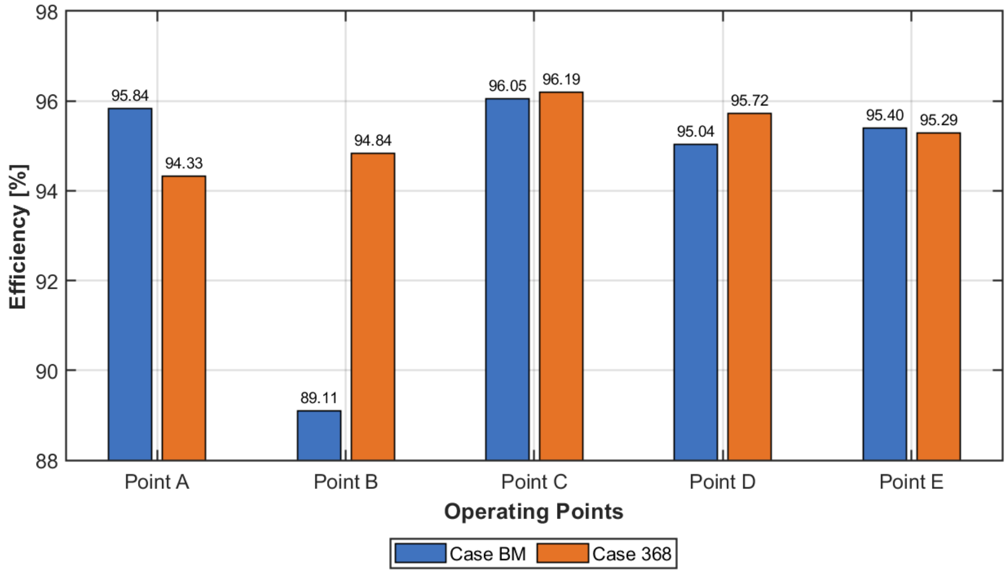

Figure 6.20: Efficiency comparison at the selected operating points.

Figure 6.20 shows that the selected candidate gives competitive efficiency compared with the benchmark machine. The efficiency is slightly lower at Point A, but it improves at Points B, C, and D, while remaining very close at Point E. This confirms that the cost reduction was not achieved by sacrificing the main energy conversion performance.

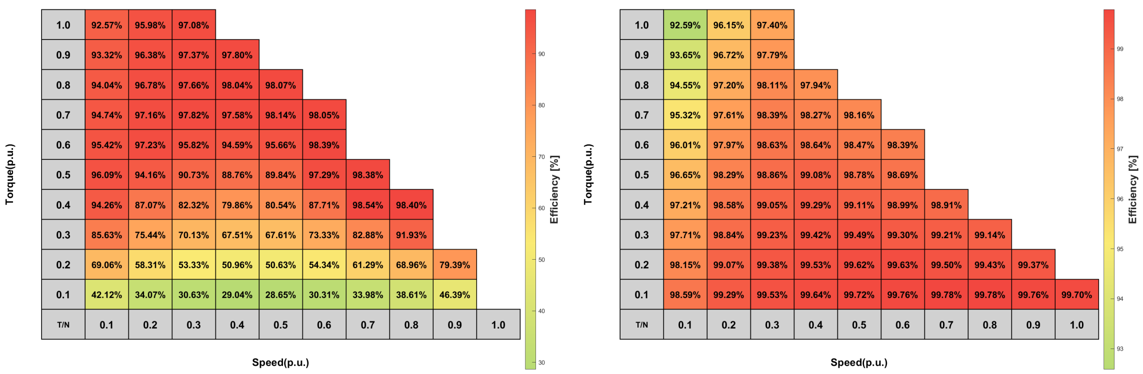

(a) Benchmark machine.

(b) Selected candidate.

Figure 6.21: Per-unit efficiency maps of the benchmark machine and the selected candidate.

Figure 6.21 provides a broader view of the efficiency distribution across the operating range. The selected candidate preserves the peak efficiency level while expanding the high-efficiency operating region over a wider torque-speed range. The improvement is particularly noticeable in low-to-medium torque operating areas, which are frequently encountered during normal driving cycles. These results indicate that the optimized design achieves the cost reduction objective without sacrificing efficiency performance.

6.6.2 Magnetic Flux Density Distribution

The magnetic flux density distribution was evaluated to compare the magnetic loading and flux paths of the benchmark machine and the selected candidate. This comparison helps identify possible saturation regions and verifies that the optimized design maintains an acceptable magnetic operating condition.

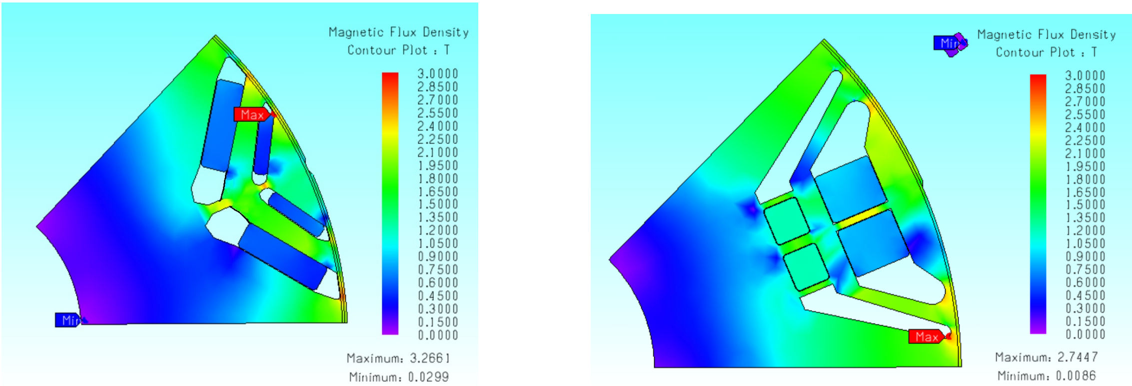

(a) Benchmark machine (VV topology).

(b) Selected candidate (Case 368).

Figure 6.22: Magnetic flux density distribution of the benchmark machine and the selected candidate at rated operating condition.

Figure 6.22 compares the magnetic flux density distribution of the benchmark machine and the selected candidate. Both designs exhibit smooth flux paths from the magnets to the stator teeth without severe localized saturation. The benchmark machine reaches a maximum flux density of approximately 3.27 T, whereas the selected candidate shows a lower peak value of approximately 2.74 T. This reduction indicates a more balanced magnetic loading and lower saturation tendency in critical rotor regions.

The selected candidate maintains an effective utilization of the magnetic material while reducing the peak flux concentration near the rotor bridges and outer rotor regions. This behavior contributes to improved electromagnetic performance and supports the robustness of the optimized design.

6.6.3 ASC Robustness Comparison

The ASC evaluation confirms that the selected candidate maintains acceptable robustness against fault-induced performance degradation. Although the benchmark machine relies on a dedicated hardware-based protection strategy, the selected candidate achieves the required robustness through topology selection and electromagnetic optimization. The obtained results demonstrate that the lower-cost magnet solution can still provide stable post-fault behavior while satisfying the robustness requirements.

6.6.4 Total E-Machine Cost Comparison

The final comparison includes both material-related cost and loss-related operating cost. The selected candidate achieves a lower total cost than the benchmark machine. Although the material cost is slightly increased, the improvement in average loss and equivalent WLTP loss compensates for this increase and leads to a more favorable overall cost value. Therefore, the selected design offers a better balance between performance and cost.

6.7 Summary of Final Improvements

Table 6.12 summarizes the final comparison between the benchmark machine and the selected candidate. The selected design corresponds to the optimized 8P-8H-72S-F45H configuration, Case 368.

Table 6.12: Final comparison between the benchmark machine and the selected candidate.

Metric	Benchmark	Selected Candidate	Improvement
Average Torque (p.u.)	1.01	1.01	Comparable
Average Efficiency (%)	94.29	95.27	+1.05%
Average Loss (p.u.)	1.00	0.95	4.83% lower
equivalent WLTP loss (p.u.)	1.00	0.95	4.83% lower
Material Cost (p.u.)	1.00	1.02	2.36% higher
Total Costs (p.u.)	1.00	0.96	3.91% lower
ASC Torque Reduction	Reference	0.92%	Acceptable robustness

The selected candidate maintains the required torque capability while improving the average efficiency and reducing the average loss and equivalent WLTP loss compared with the benchmark reference. Although the material cost is slightly higher, the lower operating-loss contribution gives a lower total costs. Therefore, the selected 8P-8H-72S-F45H Case 368 provides the best overall balance between electromagnetic performance, ASC robustness, and lifecycle-oriented cost.

Chapter 7

Conclusions

7.1 Results from present work

This thesis investigated the redesign of an automotive IPMSM using heavy rare-earth-free permanent magnet materials, with the objective of improving cost efficiency and demagnetization robustness while maintaining the required traction performance.

A systematic evaluation procedure was developed, including magnet material assessment, rotor topology screening, machine configuration analysis, and multi-stage optimization. The results showed that rotor topology has a significant influence on the balance between torque capability, efficiency, and robustness under Active Short-Circuit (ASC) conditions. Among the investigated alternatives, the segmented rotor concept demonstrated the most balanced overall behavior and provided a suitable platform for further optimization.

The study also highlighted the importance of considering magnet material properties together with electromagnetic design. While lower-cost magnet materials introduce additional challenges related to demagnetization sensitivity, appropriate rotor design and parameter optimization can effectively compensate for these limitations. The results showed that machine performance cannot be evaluated based solely on magnetic material characteristics, since the interaction between geometry, flux distribution, and operating conditions plays an equally important role.

The investigation of different pole-slot and winding configurations further demonstrated that machine architecture strongly affects both normal operating performance and fault behavior. By combining topology selection with targeted geometric modifications, it was possible to improve the trade-off between electromagnetic performance and ASC robustness without introducing additional hardware-based protection concepts.

Following the optimization process, a final candidate was selected and compared with the industrial reference machine. The comparison confirmed that the proposed design approach can maintain the required traction performance while achieving improved cost effectiveness and competitive efficiency. At the same time, the selected design demonstrated satisfactory robustness against demagnetization under severe operating conditions.

Overall, the work demonstrates that careful electromagnetic design, combined with suitable topology selection and optimization techniques, can enable the successful use of sustainable heavy rare-earth-free magnet materials in high-performance traction motor applications. The presented methodology provides a practical framework for future IPMSM development where cost, performance, and robustness must be considered simultaneously.

7.2 Future Work

The work presented in this thesis focused on the electromagnetic design, demagnetization robustness, efficiency performance, and cost-oriented optimization of the proposed machine. Although the selected design showed promising results within the scope of this study, several aspects remain of interest for future investigations.

One area for future work is the evaluation of the selected design from a mechanical perspective. Detailed structural analyses could be performed to investigate rotor stress and mechanical integrity under high-speed operating conditions. Such studies would provide additional insight into the behavior of the final design beyond the electromagnetic domain.

Another relevant extension is a more comprehensive environmental assessment of the machine. Since reducing the use of heavy rare-earth materials was one of the main motivations of this work, a dedicated environmental analysis could be carried out to quantify the sustainability benefits of the proposed design and compare them with those of the benchmark machine.

Bibliography

References

[1] @bookPyrhonen2014DesignRotatingElectricalMachines, author = Pyrhönen, Juha and Jokinen, Tapani and Hrabovcová, Valeria, title = Design of Rotating Electrical Machines, edition = 2, publisher = John Wiley & Sons, Ltd., address = Chichester, U.K., year = 2014, doi = 10.1002/9781118701591, url = https://doi.org/10.1002/9781118701591

[2] @articleGutfleisch2011MagneticMaterials, author = Gutfleisch, O. and Willard, M. A. and Brück, E. and Chen, C. H. and Sankar, S. G. and Liu, J. P., title = Magnetic Materials and Devices for the 21st Century: Stronger, Lighter, and More Energy Efficient, journal = Advanced Materials, volume = 23, number = 7, pages = 821–842, year = 2011, doi = 10.1002/adma.201002180, url = https://doi.org/10.1002/adma.201002180

[3] @inproceedingsZhao2010DemagnetizationShortCircuit, author = Zhao, G. and Tian, L. and Shen, Q. and Tang, R., title = Demagnetization Analysis of Permanent Magnet Synchronous Machines under Short Circuit Fault, booktitle = Proceedings of the Asia-Pacific Power and Energy Engineering Conference (APPEEC), address = Chengdu, China, pages = 1–4, year = 2010, doi = 10.1109/APPEEC.2010.5448459, url = https://doi.org/10.1109/APPEEC.2010.5448459

[4] @inproceedingsGhiba2024HybridMagnetIPM, author = Ghiba, S. and Raj, R. and Halder, S. and Bergsro, K. and Ferrari, S. and Pellegrino, G., title = Design of Hybrid Magnet IPM Machine for Traction Applications, booktitle = Proceedings of the 2024 International Conference on Electrical Machines (ICEM), address = Torino, Italy, pages = 1–6, year = 2024, doi = 10.1109/ICEM60801.2024.10700239, url = https://doi.org/10.1109/ICEM60801.2024.10700239

[5] @articleNiu2023RotorTopologyOptimization, author = Niu, L. and Zhang, M., title = Rotor Topology Optimization and Electromagnetic Performance Analysis of Interior Permanent Magnet Synchronous Motors for Electric Vehicle Applications, journal = The Journal of Engineering, volume = 2023, pages = 1–19, year = 2023, doi = 10.1049/tje2.12240, url = https://doi.org/10.1049/tje2.12240

[6] @inproceedingsFatemi2025IrreversibleDemagnetization, author = Fatemi, A. and Peng, P. and Gallert, B. and Hembel, A., title = Assessment of Irreversible Demagnetization in Permanent Magnet EV Motors, booktitle = Proceedings of the 2025 IEEE Energy Conversion Congress and Exposition (ECCE), address = Philadelphia, PA, USA, pages = 1–8, year = 2025, doi = 10.1109/ECCE58356.2025.11259607, url = https://doi.org/10.1109/ECCE58356.2025.11259607

[7] @techreportUNECE2021WLTP, author = United Nations Economic Commission for Europe, title = United Nations Global Technical Regulation No. 15: Worldwide Harmonized Light Vehicles Test Procedure, Amendment 6, institution = UNECE, address = Geneva, Switzerland, year = 2021, url = https://unece.org/sites/default/files/2022-06/ECE-TRANS-180a15am6e.pdf

[8] @inproceedingsNishiyama2017HighlyDemagnetization, author = Nishiyama, N. and Uemura, H. and Honda, Y., title = The Study of Highly Demagnetization Performance IPMSM under Hot Environments, booktitle = Proceedings of the 20th International Conference on Electrical Machines and Systems (ICEMS), address = Sydney, NSW, Australia, pages = 1–6, year = 2017, doi = 10.1109/ICEMS.2017.8056505, url = https://doi.org/10.1109/ICEMS.2017.8056505

[9] @bookKrause2013ElectricMachinery, author = Krause, Paul C. and Wasynczuk, Oleg and Sudhoff, Scott D. and Pekarek, Steven D., title = Analysis of Electric Machinery and Drive Systems, edition = 3, publisher = Wiley-IEEE Press, address = Hoboken, NJ, USA, year = 2013, doi = 10.1002/9781118524336, url = https://doi.org/10.1002/9781118524336

[10] @bookBoldea1996Reluctance, author = Boldea, Ion, title = Reluctance Synchronous Machines and Drives, publisher = Clarendon Press, address = Oxford, UK, year = 1996, isbn = 9780198593911, doi = 10.1093/oso/9780198593911.001.0001, url = https://doi.org/10.1093/oso/9780198593911.001.0001

[11] @phdthesisLi2020AdvancedFluxWeakening, author = Li, Yihui, title = Advanced Flux-Weakening Control Methods for Interior Permanent Magnet Synchronous Motors with Torque Performance Improvement, school = McMaster University, address = Hamilton, ON, Canada, year = 2020, type = Ph.D. dissertation, url = https://hdl.handle.net/11375/25592

[12] @bookKrishnan2010PMSM, author = Krishnan, Ramu, title = Permanent Magnet Synchronous and Brushless DC Motor Drives, publisher = CRC Press, address = Boca Raton, FL, USA, year = 2010, doi = 10.1201/9781420014235, url = https://doi.org/10.1201/9781420014235

[13] @phdthesisKrings2014IronLosses, author = Krings, Andreas, title = Iron Losses in Electrical Machines: Influence of Material Properties, Manufacturing Processes, and Inverter Operation, school = KTH Royal Institute of Technology, address = Stockholm, Sweden, year = 2014, type = Ph.D. dissertation, url = https://urn.kb.se/resolve?urn=urn:nbn:se:kth:diva-145243

[14] @articleToda2004RotorEddyCurrentLoss, author = Toda, H. and Xia, Z. and Wang, J. and Atallah, K. and Howe, D., title = Rotor eddy-current loss in permanent magnet brushless machines, journal = IEEE Transactions on Magnetics, volume = 40, number = 4, pages = 2104–2106, month = jul, year = 2004, doi = 10.1109/TMAG.2004.832481, url = https://doi.org/10.1109/TMAG.2004.832481

[15] @articleZhou2012TemperatureDependentDemagnetization, author = Zhou, P. and Lin, D. and Xiao, Y. and Lambert, N. and Rahman, M. A., title = Temperature-Dependent Demagnetization Model of Permanent Magnets for Finite Element Analysis, journal = IEEE Transactions on Magnetics, volume = 48, number = 2, pages = 1031–1034, month = feb, year = 2012, doi = 10.1109/TMAG.2011.2172395, url = https://doi.org/10.1109/TMAG.2011.2172395

[16] @phdthesisGanchev2013SensorlessRotorMagnetTemperature, author = Ganchev, Martin D., title = Sensorless Rotor Magnet Temperature Estimation of Permanent Magnet Synchronous Motors, school = Technische Universität Wien, address = Vienna, Austria, year = 2013, type = Ph.D. dissertation, doi = 10.34726/hss.2013.23477, url = https://doi.org/10.34726/hss.2013.23477

[17] @articleOlson2024ActiveShortCircuit, author = Olson, G. F. and Bojoi, A. and Pescetto, P. and Ferrari, S. and Peretti, L. and Pellegrino, G., title = Active Short-Circuit Strategy

for PMSMs Enabling Bounded Transient Torque and Demagnetization Current, journal = IEEE Access, volume = 12, pages = 109001–109011, year = 2024, doi = 10.1109/ACCESS.2024.3440015, url = https://doi.org/10.1109/ACCESS.2024.3440015

[18] @techreportIEA2024CriticalMineralsOutlook, author = International Energy Agency, title = Global Critical Minerals Outlook 2024, institution = IEA, address = Paris, France, year = 2024, url = https://www.iea.org/reports/global-critical-minerals-outlook-2024

A

Material specification

All material definitions used in this work were implemented directly in JMAG. The properties were either obtained from the built-in material library or defined according to reference motor data to ensure consistency with the benchmark model.

A.1 Copper

The material properties of copper used in this study were taken from the SysLibrary database available in JMAG. The copper material was modeled as an isotropic conductive material with temperature-dependent characteristics defined at the reference operating condition. These properties were directly implemented in the electromagnetic simulations to accurately represent winding behavior under load.

A.2 N42UH

The N42UH magnet was used as the reference magnet material in the benchmark motor model. This grade provides high temperature capability and strong demagnetization resistance, which makes it suitable as a baseline for comparison with the HREE-free candidate magnets. The B-H characteristics used in the simulations are shown in Figure A.1.

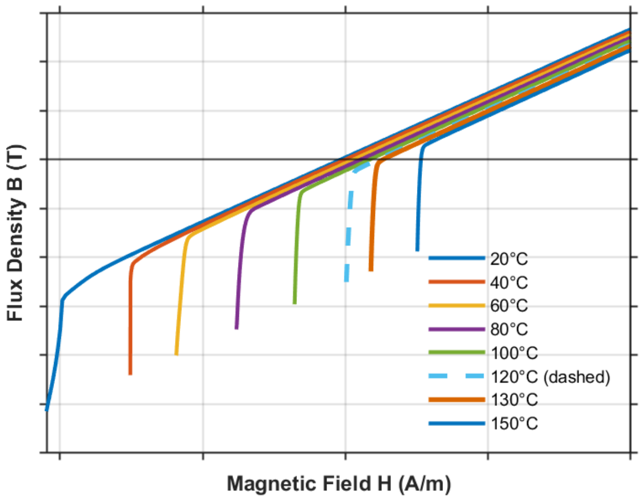

Figure A.1: B-H curve of the N42UH magnet at different temperatures.

A.3 Electrical Steel

The electrical steel material used for both stator and rotor cores corresponds to the Thyssen grade. The magnetic and mechanical properties were defined in JMAG based on manufacturer data and validated reference sources. In particular, the B–H curve and core loss characteristics were imported into the software to ensure a reliable prediction of magnetic saturation and iron losses under transient operating conditions. This material definition was used consistently across all simulation cases.

DEPARTMENT OF Electrical Engineering
Division of Electric Power Engineering
CHALMERS UNIVERSITY OF TECHNOLOGY
Gothenburg, Sweden 2026
www.chalmers.se